Simulating heat and CO_2 fluxes in Beijing using SUEWS V2020b: Sensitivity to vegetation phenology and maximum conductance

Yingqi Zheng[1,2,4], Minttu Havu[2], Huizhi Liu[3], Xueling Cheng[1,4], Yifan Wen[5], Hei Shing Lee[2,6], Joyson Ahongshangbam[2], and Leena Järvi[2,6]

[1]State Key Laboratory of Atmospheric Boundary Layer Physics and Atmospheric Chemistry, Institute of Atmospheric Physics, Chinese Academy of Sciences, Beijing, 100029, China
[2]Institute for Atmospheric and Earth System Research/Physics, Faculty of Science, University of Helsinki, Helsinki, 00560, Finland
[3]Department of Atmospheric Sciences, Yunnan University, Kunming, 650091, China
[4]College of Earth and Planetary Sciences, University of Chinese Academy of Sciences, Beijing, 100029, China
[5]School of Environment, State Key Joint Laboratory of Environment Simulation and Pollution Control, Tsinghua University, Beijing, 100084, China
[6]Helsinki Institute of Sustainability Science, University of Helsinki, Helsinki, 00560, Finland

Correspondence: Huizhi Liu (huizhil@mail.iap.ac.cn)

Abstract. The Surface Urban Energy and Water Balance Scheme (SUEWS) has recently been introduced to include a bottom-up approach to modelling carbon dioxide (CO_2) emissions and uptake in urban areas. In this study, SUEWS is evaluated against the eddy covariance (EC) measured turbulent fluxes of sensible heat (Q_H), latent heat (Q_E), and CO_2 (F_C) at a densely built neighborhood in Beijing. The model sensitivity to maximum conductance (g_{max}) and leaf area index (LAI) is examined. Site-specific g_{max} is obtained from observations over local vegetation species, and LAI parameters by optimization with remotely sensed LAI obtained from a Landsat 7 data product. For the simulation of anthropogenic CO_2 components, local traffic and population data are collected. In the model evaluation, the mismatch between the measurement source area and simulation domain is also considered.

Using the optimized g_{max} and LAI, the modelling of heat fluxes is noticeably improved, showing higher correlation with observations, lower bias, and more realistic seasonal dynamics of Q_E and Q_H. The effect of the g_{max} adjustment is more significant than the LAI adjustment. Compared to heat fluxes, the F_C module shows lower sensitivity to the choices of g_{max} and LAI. This can be explained by the low relative contribution of vegetation to the net F_C in the modelled area. SUEWS successfully reproduces the average diurnal cycle of F_C and annual cumulative sums. Depending on the size of the simulation domain, the modelled annual accumulated F_C ranges from 7.4 to 8.7 kg C m^{-2} yr^{-1}, when compared to 7.5 kg C m^{-2} yr^{-1} observed by EC. Traffic is the dominant CO_2 source, contributing 59–70% to the annual total CO_2 emissions, followed by human metabolism (14–18%), buildings (11–14%), and CO_2 release by vegetation and soil respiration (6–10%). Vegetation photosynthesis offsets only 5–10% of the total CO_2 emissions. We highlight the importance of choosing the optimal LAI parameters and g_{max} when SUEWS is used to model surface fluxes. The F_C module of SUEWS is a promising tool in quantifying urban CO_2 emissions at the local scale, and therefore assisting to mitigate urban CO_2 emissions.

1 Introduction

Currently, half of the global population resides in urban areas, and this percentage is projected to grow to 68% by the middle of the 21st century (United Nations Department of Economic and Social Affairs, 2019). Urban expansion has reshaped the morphological, thermal, and dynamical properties of the land surface (Grimmond and Oke, 2006; Oke, 1995; Zhu et al., 2016). In addition, intensive human activities in urban areas have caused a large quantity of greenhouse gas emissions (Marcotullio et al., 2013; Velasco and Roth, 2010). Both factors have influenced urban climate from micro to regional scales (Johansson and Emmanuel, 2006; Sarangi et al., 2018; Tan et al., 2010). Climatic and environmental risks due to urbanization are frequently reported, such as heat waves, flooding, and air pollution (Qian et al., 2022; Watts et al., 2015). In this context, there is a pressing need to better understand the effects of urbanization on land-atmosphere interaction, preferably in a quantitative way.

Urban land surface models (ULSMs) are widely used to simulate urban-atmosphere interactions, including the exchanges of energy, water, and CO_2, and hydrological processes (Chen et al., 2011; Masson et al., 2013). The results from the First International Urban Land Surface Model Comparison Project suggested that the most important processes for urban surface energy balance were radiative and vegetation processes (e.g., vegetation fraction, seasonal cycle of vegetation phenology) (Best and Grimmond, 2015; Grimmond et al., 2010; Nordbo et al., 2015). Long-term observations with low vegetation cover ($<$30%) were especially needed to evaluate heat flux simulation, as energy distribution was found sensitive in such environments (Best and Grimmond, 2016).

The Surface Urban Energy and Water balance Scheme (SUEWS) is one of the widely tested ULSMs (Järvi et al., 2011, 2014; Ward et al., 2016). SUEWS is designed to run with surface information (e.g., surface cover fractions) and a minimum amount of model forcing data. In recent years, Supy (SUEWS in Python) was developed to allow Python front-end implementation for broader and easier applications (Sun and Grimmond, 2019). SUEWS has demonstrated good performance against hydrological observations and surface flux observations in several cities in Europe, North America, and Asia (Alexander et al., 2016; Ao et al., 2018; Havu et al., 2022a; Järvi et al., 2011; Ward et al., 2016). In SUEWS, the seasonal cycle of vegetation phenology is indicated by leaf area index (LAI). Previous studies made in two UK cities and Shanghai, China have reported that bias in modelled LAI lead to over- or underestimation in Q_E or Q_H (Ao et al., 2018; Ward et al., 2016). They highlighted the importance of having an appropriate seasonal cycle of LAI in SUEWS. Omidvar et al. (2022) proposed a workflow to derive LAI-related parameters for SUEWS, but it was intended for fully vegetated areas located mainly on the outskirt of cities. Apart from LAI, the maximum conductance (g_{max}) is also critical in scaling the surface conductance (g_s), and therefore the available energy distribution (Ward et al., 2016). However, the impact of LAI-related parameters and g_{max} on the modelled turbulent fluxes has received insufficient attention in urban areas.

Recently, the module of local-scale CO_2 flux (F_C) was incorporated into SUEWS (Järvi et al., 2019). It was found to give reasonable annual sum, seasonal and diurnal cycles against observed F_C in Helsinki, Finland, suggesting that the bottom-up CO_2 emission or uptake estimate in SUEWS can be evaluated by observation-based evidence provided by top-down eddy covariance (EC) measurements. Furthermore, SUEWS shows the potential for broader use, such as quantifying the carbon sequestration potential of urban vegetation (Havu et al., 2022a), investigating the spatial variability of CO_2 emission, quanti-

fying the contribution of each emission component (Järvi et al., 2019), and therefore assisting urban CO_2 emission mitigation. However, this module has not yet been evaluated in other cities than Helsinki.

Beijing provides a unique test-bed for SUEWS evaluation and application: a mega-city with a population of over 21 million and an increasing urbanized area (MHURD, 2018). The older version of SUEWS (V2017b), has been evaluated and applied in Beijing by Kokkonen et al. (2019), showing good model performance against observed heat fluxes. However, good simulation of turbulent flux does not necessarily imply that the sub-models within give accurate estimates, e.g., LAI and radiative components. Correct presentation of these processes is necessary for more advanced applications such as the prediction of surface exchanges of energy under e.g., future climate scenarios. Besides, the newly-developed F_C module has not yet been evaluated in Beijing.

In this paper, we present a comprehensive evaluation of SUEWS V2020b in simulating surface fluxes of energy and CO_2 in Beijing. The main aims of this study are (1) to evaluate the model performance of SUEWS using different vegetation parameters (default and site-specific) against the turbulent flux (Q_E, Q_H and F_C) measurements, and (2) to estimate the anthropogenic and biogenic components' contributions to the F_C with the bottom-up modelling approach by SUEWS. Meanwhile, the impact of the mismatch between the turbulent flux source area and the modelled area is also examined.

2 Model Description

SUEWS is an urban land surface model that simulates the surface energy and water balances, and CO_2 flux at a local (neighborhood) scale (Järvi et al., 2011, 2019; Ward et al., 2016). In SUEWS, the modelling domain is separated into seven interacting surface types (buildings, paved surfaces, grass, evergreen trees/shrub, deciduous trees/shrubs, bare soil, and water body), with a single soil layer below each type. SUEWS is designed to run with surface information (e.g., surface cover fractions) and a minimal amount of model forcing data including wind speed (U), relative humidity (RH), air temperature (T_{air}), air pressure (p), precipitation and incoming solar radiation (K_{down}). SUEWS has sub-models for LAI and net all-wave radiation, and users are allowed to modify the parameters of the sub-models based on the information of the modelled domain. In this study, we use SUEWS version V2020b (Havu et al., 2022b).

2.1 Leaf area index model

In SUEWS, leaf growth is accumulated when T_{air} stays above the limit value $T_{base,GDD,i}$ consecutively, denoted by growing-degree-day (GDD). Leaf growth is allowed until GDD reaches the upper boundary $GDD_{full,i}$ or LAI reaches its maximum ($LAI_{max,i}$). Similarly to the leaf growth period, the leaf off period is impacted by $T_{base,SDD,i}$, senescence-degree-day (SDD), and $SDD_{full,i}$ or $LAI_{min,i}$. Leaf fall is controlled by T_{air} or at high latitudes by day length (Järvi et al., 2014). Here, LAI for vegetation type i at the day of year d ($LAI_{d,i}$) is defined as:

$$LAI_{d,i} = \begin{cases} \min\left(LAI_{max,i}, LAI_{d-1,i}^{\omega_1,GDD,i} \cdot GDD_{d,i} \cdot \omega_{2,GDD,i} + LAI_{d-1,i}\right), \text{leaf-on}, T_{base,GDD,i} > T_{d-1} \\ \max\left(LAI_{min,i}, LAI_{d-1,i}^{\omega_1,SDD,i} \cdot SDD_{d,i} \cdot \omega_{2,SDD,i} + LAI_{d-1,i}\right), \text{leaf-off}, T_{d-1} < T_{base,SDD,i}, \end{cases} \quad (1)$$

where $LAI_{max,i}$ and $LAI_{min,i}$ for each vegetation type can be obtained from literature or determined from observations, $\omega_{1/2,GDD/SDD,i}$ represent the growing or senescence rates derived for each study site or use their default values (Järvi et al., 2011; Omidvar et al., 2022), and T_{d-1} is the previous day air temperature mean.

2.2 Radiation fluxes

K_{down} is a required variable in the meteorological forcing data, whereas other radiation components are estimated within SUEWS. Outgoing shortwave radiation (K_{up}) is calculated using a bulk albedo (α) based on the area fraction for each surface type. Incoming longwave radiation (L_{down}) is calculated using T_{air} and RH to estimate the cloud cover and the clear-sky emissivity (Loridan et al., 2011), while outgoing longwave radiation (L_{up}) is estimated by surface emissivity, α, K_{down}, L_{down} and T_{air} (Offerle et al., 2003).

2.3 Turbulent heat fluxes

Latent heat flux (Q_E, W m^{-2}) is calculated using the modified Penman-Monteith equation for each surface type:

$$Q_E = \frac{s(Q_N + Q_F - \Delta Q_s) + \rho c_p VPD/r_{av}}{s + \gamma(1 + r_s/r_{av})}, \quad (2)$$

where Q_N (W m^{-2}) is the net all-wave radiation, Q_F (W m^{-2}) the anthropogenic heat flux, ΔQ_S (W m^{-2}) the net storage heat flux, ρ (kg m^{-3}) the air density, c_p (J kg^{-1} K^{-1}) the specific heat capacity of air at constant pressure, VPD (Pa) the vapour pressure deficit, s (Pa °C^{-1}) the slope of the saturation vapour pressure curve, γ (Pa °C^{-1}) the psychrometric constant, r_{av} (s mm^{-1}) the aerodynamic resistance for water vapour, and r_s (s mm^{-1}) the surface resistance. r_s, or its inverse surface conductance g_s (mm s^{-1}), has the form:

$$g_s = \frac{1}{r_s} = \sum_i (g_{max,i} \frac{LAI_i}{LAI_{max,i}} fr_i) G_1 g(K_{down}) g(\Delta q) g(T_{air}) g(\Delta\theta), \quad (3)$$

where $g_{max,i}$ is the maximum conductance of vegetation type i, fr_i is the surface fraction of i, G_1 is a constant connecting stomatal conductance to canopy conductance, $g(K_{down})$, $g(\Delta q)$, $g(T_{air})$, and $g(\Delta\theta)$ are environmental response functions on K_{down}, specific humidity deficit (Δq), air temperature (T_{air}), and soil moisture deficit ($\Delta\theta$), respectively. The functions have the forms (Ward et al., 2016):

$$g(K_{down}) = \frac{K_{down}/(G_2 + K_{down})}{K_{down,max}/(G_2 + K_{down,max})}, \quad (4)$$

$$g(\Delta q) = G_3 + (1 - G_3) G_4^{\Delta q}, \quad (5)$$

$$g(T_{air}) = \frac{(T_{air} - T_L)(T_H - T_{air})^{T_C}}{(G_5 - T_L)(T_H - G_5)^{T_C}}, \tag{6}$$

where

$$T_C = \frac{(T_H - G_5)}{(G_5 - T_L)}, \tag{7}$$

and

$$g(\Delta\theta) = \frac{1 - \exp(G_6(\Delta\theta - \Delta\theta_{WP}))}{1 - \exp(-G_6\Delta\theta_{WP})}. \tag{8}$$

Coefficients $G_2 - G_6$ determine the shape of the curves describing responses of stomatal conductance to each environmental variable. $K_{down,max}$ (W m^{-2}) is the maximum incoming solar radiation, T_L and T_H (°C) are the lower and upper limits for temperature at which photosynthesis and transpiration are off, and $\Delta\theta_{WP}$ (mm) is wilting point deficit. K_{down} (W m^{-2}) is model input, Δq (g kg^{-1}) is calculated from model input RH, T_{air} (°C) is either model input or simulated at 2 m height, and $\Delta\theta$ (mm) is simulated within SUEWS (Järvi et al., 2017). Q_H is determined as the residual from the surface energy balance equation:

$$Q_H = Q_N + Q_F - \Delta Q_S - Q_E. \tag{9}$$

2.4 CO_2 flux

The F_C module adopts a bottom-up approach to determine the local-scale F_C (μmol m^{-2} s^{-1}), accounting for both anthropogenic ($F_{C,ant}$) and biogenic ($F_{C,bio}$) components (Järvi et al., 2019):

$$F_C \quad = \quad F_{C,ant} + F_{C,bio} = (F_M + F_V + F_B + F_P) + (F_{pho} + F_{res}) \ . \tag{10}$$

In the Eq. 10, F_M are the CO_2 emissions from human metabolism, F_V the emissions from traffic, F_B the emissions from buildings (e.g., combustion of natural gas, coal, and wood), F_P the emissions from local-scale point sources, F_{pho} the CO_2 uptake by photosynthesis, and F_{res} the CO_2 release by soil and vegetation respiration. Positive values indicate CO_2 emissions and negative values indicate CO_2 uptake with respect to the atmosphere. F_{pho} has a negative sign while the rest of the F_C components have a positive sign.

$F_{C,ant}$ relates to the energy balance through Q_F. F_M and F_V are estimated with an inventory approach, i.e., based on population density or traffic rate, and their emission factors (EFs). Hourly CO_2 emissions from human metabolism on weekdays or weekends ($F_{M,h,d}$, μmol m^{-2} s^{-1}) are calculated using:

$$F_{M,h,d} = p_d \cdot PP_{h,d} \cdot AP_{h,d} \cdot C_M, \tag{11}$$

where p_d is the daily average population density (cap ha^{-1}), $PP_{h,d}$ the population diurnal profile by hour, $AP_{h,d}$ the activity level diurnal profile by hour, and C_M the CO_2 release per person (μmol CO_2 s^{-1} cap^{-1}). The p_d and $PP_{h,d}$ reconstruct the

diurnal population density cycle. $AP_{h,d}$ scales the C_M to vary between the nighttime minimum and daytime maximum values ($C_{M(min,max)}$) to indicate the diurnal cycle of per capita human metabolic intensity.

Hourly traffic CO_2 emissions ($F_{V,h,d}$) on weekdays or weekends are calculated from

$$F_{V,h,d} = Tr_d \cdot E_{c,d} \cdot H_{T,d}, \tag{12}$$

where Tr_d is the mean daily traffic rate within the study area (veh day^{-1} area^{-1}), $H_{T,d}$ the diurnal traffic profiles, and $E_{c,d}$ the traffic the EFs for CO_2 (kg km^{-1} veh^{-1}).

Hourly building CO_2 emissions ($F_{B,h,d}$) on weekdays or weekends are calculated from

$$F_{B,h,d} = [fr_{heat} \cdot Q_{F,heat} + fr_{nonheat} \cdot Q_{F,base} \cdot fr_{QF,base,BEU,d}] \cdot E_{CO2perJ}, \tag{13}$$

where fr_{heat} is the fraction of fossil fuels used for heating, $Q_{F,heat}$ the building heat emission at local scale estimated from the heating-degree-day model (Järvi et al., 2011), $fr_{nonheat}$ the fraction of fossil fuels used for energy other than heating (e.g. the use of gas stove for cooking), $Q_{F,base}$ the non-temperature related anthropogenic heat flux (W m^{-2}) including heat emissions from traffic, human metabolism, and electricity usage, $fr_{QF,base,BEU,d}$ the fraction of the $Q_{F,base}$ coming from building energy use on weekdays or weekends, and $E_{CO2perJ}$ the EF for fuels in building energy use (μmol CO_2 J^{-1}). Emissions from single-point sources such as power plants and industrial activities can be included as model inputs.

F_{pho} relates to the energy balance through LAI and the environmental responses of surface conductance (Eq. 3). F_{pho} is calculated using

$$F_{pho} = \sum_i (fr_i F_{pho,max,i} LAI_i) g(T_{air}) g(\Delta q) g(\Delta\theta) g(K_{down}), \tag{14}$$

where $F_{pho,max,i}$ is the maximum photosynthetic rate for vegetation type i.

Soil and vegetation respiration F_{res} (μmol m^{-2} s^{-1}) follows an exponential dependency on T_{air}:

$$F_{res} = \sum_i fr_i \max(a_i \cdot \exp(T_{air} b_i), 0.6), \tag{15}$$

where a_i and b_i are the parameters controlling the temperature dependency, and 0.6 μmol m^{-2} s^{-1} is the minimum respiration in winter time.

3 Study site and measurements

The model domain is a 1 km circle around the 325 m meteorological tower constructed by Institute of Atmospheric Physics, Chinese Academy of Sciences (IAP tower, 39°58' N, 116°22' E, 60 m above sea level) located in the 6th Ring area of Beijing, China (Fig. 1 a–d). An EC setup at the height of 47 m on IAP tower continuously measures the surface fluxes of Q_E, Q_H and F_C using a 3-dimensional sonic anemometer (Windmaster, Gill, UK) and an open-path infrared gas analyzer (LI-7500A, LI-COR, USA). In addition, all four radiation components are measured at the height of 140 m using a net radiometer (CNR1,

Kipp & Zonen, Netherlands). These measurements are used to evaluate SUEWS model performance. The 1 km radius circle around IAP tower roughly covers 80% accumulated flux footprint area (Liu et al., 2012). This area is mainly covered by impervious surfaces (Fig. 1 b). Three patches of urban green spaces are situated to the east, south, and west to IAP tower, while the other vegetation is scarcely located along the roads and near the buildings. Most of the impervious surfaces in the source area are residential buildings (Fig. 1 d). A more detailed description of the surroundings and the used instruments can be found in the previous publications by Cheng et al. (2018), Liu et al. (2012), and Liu et al. (2021).

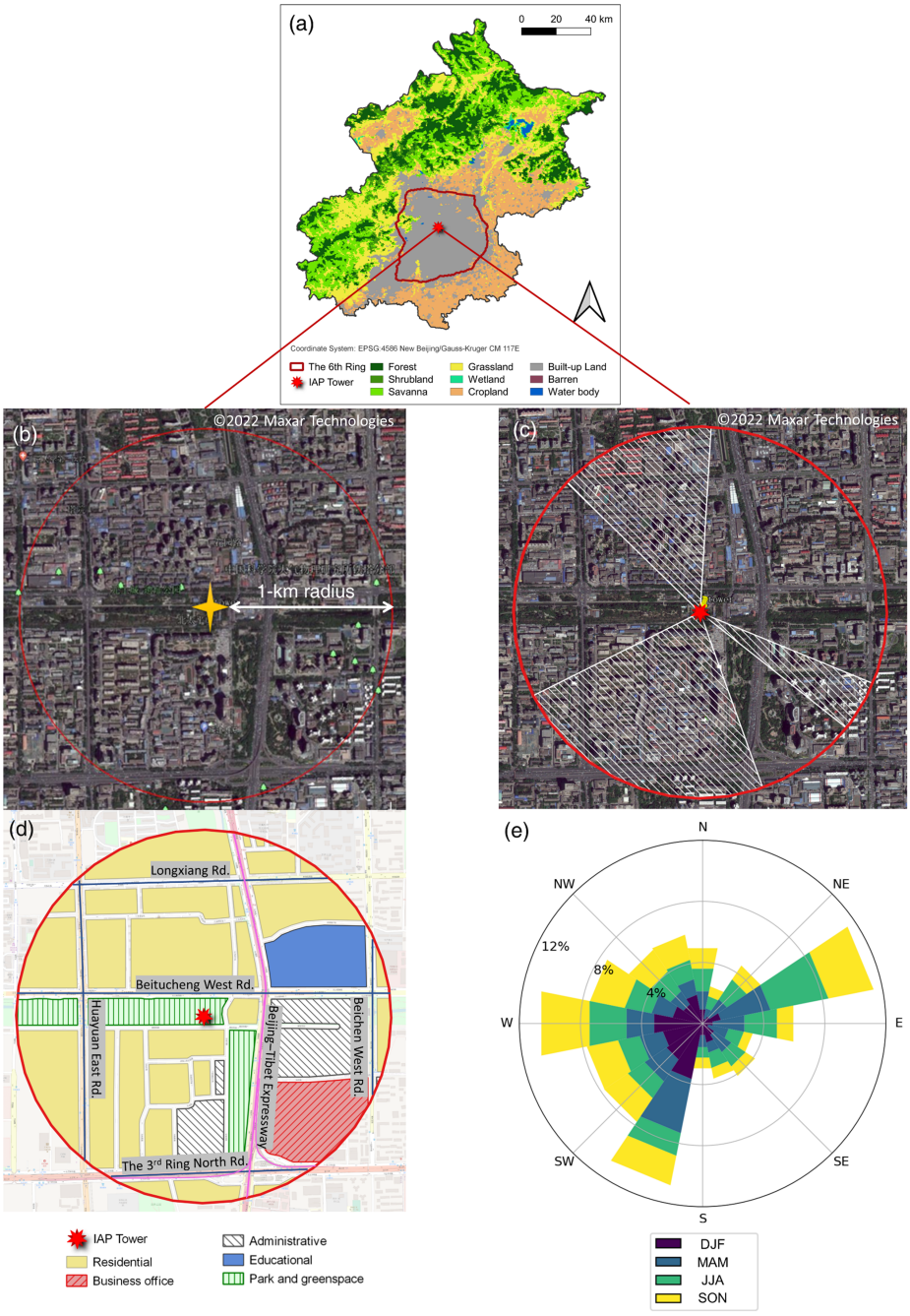

Figure 1. (a) The location of IAP tower and the land cover type within the 6th Ring area of Beijing (MODIS Land Cover Type (MCD12Q1) Version 6, Friedl and Sulla-Menashe (2019)), (b) a satellite image (Google Earth, image ©2022 Maxar Technologies) over the study area, (c) wind sectors that have been filtered out for data quality control, (d) urban land use categories (EULUC-China) (Gong et al., 2020), and (e) wind direction frequency by season.

The 30-min turbulent flux calculation procedures and the quality controls were described in detail by Cheng et al. (2018). Quality controls such as out-of-limit value removal, spike removal, and a dropout test were conducted on the 10 Hz data during the flux calculation. In order to exclude low-quality data caused by precipitation, dust, or other contamination on the sensor, the records with automatic gain control value ≥ 62 were discarded. On top of the procedures by Cheng et al. (2018), the following quality control steps are performed for 30-minute turbulent flux observations in the year 2016. (1) Upper/lower boundary filtering: Q_E observations that fall outside the range from -500 to 1000 W m^{-2}, Q_H from -500 to 1000 W m^{-2}, and F_C from -100 to 200 μmol m^{-2} s^{-1} are removed. (2) Spikes detection: flux values outside 3.5 times of the standard deviation from the 3-day moving mean value are removed (Liu et al., 2012). (3) Wind direction filtering: the wind directions with building heights over 50 m (112–128, 160–243, 314–3°) are removed (Kokkonen et al., 2019) (Fig. 1 c). (4) Stationarity test: data points with stationary indicator $> 30\%$ are filtered out (Foken and Wichura, 1996). The percentages of data removed through these 4 steps are 0.2–0.3%, 1.7–2.7%, 37.8–38.2%, and 13.1–17.4%, respectively. The numbers of observations retained after quality control are 8017 for Q_E, 7338 for Q_H, and 7797 for F_C. These 30-minute flux observations are resampled to one–hour resolution. In addition, F_C is gap-filled using seasonal mean diurnal cycle in order to calculate the seasonal and annual sums (Falge et al., 2001).

Wind directions are mainly from the S-W sectors and the NE-E sectors before the implementation of the wind direction filtering (Fig. 1 e). In winter, wind from the west is more frequently seen than from the east compared to the other seasons.

To optimize the behavior of LAI, a six-year time series (2011–2016) of LAI over an adjacent park near IAP tower is calculated from the atmospherically corrected surface reflectance provided by USGS Landsat 7 Enhanced Thematic Mapper + (ETM+) (30 m spatial resolution) via the Google Earth Engine Data Catalog (Masek et al., 2006). The atmospherically corrected surface reflectance bands have been preprocessed using the scaling factors from the metadata. Next, enhanced vegetation index (EVI) is calculated using the formula (Huete, 1997):

$$EVI = 2.5 \times (NIR - RED) / (NIR + 6 \times RED - 7.5 \times BLUE + 1), \tag{16}$$

where NIR, RED and BLUE are the near-infrared, red, and blue bands, respectively. EVI is further used to calculate LAI with the formula (Boegh et al., 2002):

$$LAI = 3.618 \times EVI - 0.118. \tag{17}$$

The LAI and air temperature time series are subjected to optimization using the Covariance matric adaptation evolution strategy (CMA-ES) (Appendix A). Before the optimization process, values larger than 10 m^2 m^{-2} and negative values are considered as outliers and removed; values during December and January are set to a fixed value, i.e., the average of these months (0.2 m^2 m^{-2}), to reduce the noise in winter and improve the optimization performance. More details can be found at Appendix A. The related data and codes are openly available to reproduce the results (Zheng et al., 2022).

4 Model run

4.1 Forcing meteorological data

The reanalysis dataset WFDE5 (Cucchi et al., 2021) is used as the forcing data for SUEWS. WFDE5 is a bias-corrected dataset of near-surface meteorological variables specifically suited for land surface modelling. It is derived from the fifth generation of the European Centre for Medium-Range Weather Forecasts (ECMWF) atmospheric reanalysis (Hersbach et al., 2020). It is provided at 0.5° spatial and at hourly temporal resolution. WFDE5 is evaluated against observed meteorological observations before it is used as the forcing data for SUEWS (Appendix B).

4.2 Land cover

Land cover types and their fractions needed in the model cases are estimated based on aerial images. Paved surface accounts for 46% of the total area, buildings 24%, trees/shrub 13%, grass/lawn 16%, and water 1%. The average building height is 19.1 m (Kokkonen et al., 2019). According to a field survey conducted in the 6th Ring area, the population of deciduous species accounts for 82% of the total number of woody plants investigated (Ma, 2019). Therefore, the surface fraction of deciduous trees is set to 11% and evergreen trees 2%.

Due to the wind direction filtering (Sect. 3), the actual flux source area "seen" by the EC measurement is biased from the 1 km radius circle around IAP tower. The vegetation fraction is 31% in the remaining sectors combined, as compared to 29% in the entire 1 km radius circle (Fig. 1 b–c, Table S1). The model performance in turbulent flux modelling with the land fractions for the remaining sectors is similar to the entire circle (Fig. S1). Therefore, only the results using the land fractions of the entire circle are demonstrated in the main text.

4.3 Storage heat flux

To calculate the storage heat flux, Objective Hysteresis Model (OHM) is used (Grimmond and Oke, 1999). The coefficients for all the surface types follow the previous study by Kokkonen et al. (2019). A large portion of the paved surface is asphalt in the study area. Thus, the coefficients are set to the weighted average values of asphalt surface (AN99) following Ward et al. (2016).

4.4 Human activity

In this study, local parameters of traffic, population dynamics, and building energy use are incorporated in order to estimate Q_F and CO_2 emissions.

The annual mean weekday and weekend diurnal cycle of traffic rate for each road link in 2017 in the study domain are extracted from a dataset based on an extensive road traffic monitoring network (Yang et al., 2019). For weekends and weekdays, the diurnal traffic cycles are calculated independently. The total hourly traffic rate (veh km hour^{-1}) is calculated as the sum of the traffic rates, i.e., the product of traffic volume (veh hour^{-1}) and the road link length (km) from all the road links in the

study area. The hourly traffic rates are then summed up to the total daily traffic rates (veh km^{-1} day^{-1}), and divided by the total modelling area, yielding Tr_d. Finally, the diurnal traffic profiles ($H_{T,d}$) are obtained by normalizing the diurnal cycles of the total hourly traffic rate (Table 1, Fig. 2).

Annual average diurnal cycle of population density within the model domain is obtained from a dataset of hourly population dynamics at 500-m resolution generated from remotely sensed and geospatial data over the years 2015 and 2016 (Zhao et al., 2021) (Fig. 2). As there are several residential building areas located within the model domain (Fig. 1 d), population density increases in the evening when residents get home from work, remains high throughout the night, and decreases in the morning. Weekdays and weekends share the same diurnal cycle of population density in our study.

Heating in Beijing is dominated by central heating, supplied mainly at the district level. The sources include cogeneration plants fueled by coal or gas, and district boilers powered by coal, oil, or gas. Cogeneration plants are usually located at suburban or rural areas, and there are no cogeneration plants within the model domain, so their contribution to CO_2 emission is neglected in this study. In comparison, boiler plants are very common: over 5000 coal-fired and 1000 gas-fired heating boilers are located surrounding the populated areas in 2014 (Cui et al., 2019). We investigated the boiler plants near IAP tower through interviews and found that there were at least 11 of them located at multiple directions within 1.5 km distance from IAP tower. For the known boiler plants, 8 of them have a chimney height lower than 20 m. Thus, their CO_2 emissions are very likely to be observed by EC at 47 m during the heating season. Unfortunately, the heating capacity and detailed information regarding the fuel combustion for each boiler plant are unknown or restricted from access. Therefore, it is challenging to treat the boiler CO_2 emissions as point sources. As an alternative, SUEWS first estimates the anthropogenic heat release from heating $Q_{F,heat}$ and then converts the heat into local CO_2 release using the EF and the fraction of fossil fuels used for heating fr_{heat} (Eq. 13).

In 2015, the ratio of district boilers heating capacity to cogeneration plants was 4.2:1 (Zhang et al., 2019). Correspondingly, fr_{heat} is set to 0.81 to represent the heating capacity from local boiler plants. The value of natural gas consumption over the annual total heating supply is 3.2×10^6 ton coal equivalent (tce) and the value for coal consumption 2.6×10^6 tce in 2015. The consumption of the rest of the fuel types is only 3.8×10^5 tce (MHURD, 2018). The EFs of heating supply are 96.51 Tg CO_2/10^{19} J for coal-fired boiler, and 56.17 Tg CO_2/10^{19} J for gas-fired boiler, respectively (Du et al., 2018). Therefore, the EF for fuels used in building energy use ($E_{CO2perJ}$) in SUEWS takes the average of the EFs of natural gas and coal weighted by their annual consumption, i.e., 0.1688 μmol CO_2 J^{-1} (Table 1). In addition, SUEWS needs a temperature limit (base temperature, T_{base_HC}) to indicate when heating takes place in the heating-degree-day model. Central heating usually starts around 15th of November and lasts until 15th of March, when the outdoor air temperature is around 12 °C. Therefore, this value is given to SUEWS T_{base_HC} to replace the default value (18.2 °C) (Järvi et al., 2011).

Statistics showed that urban household living consumed liquefied petroleum gas 27.9×10^7 kg of coal equivalent (kgce), gas 17.1×10^8 kgce, and electricity 20.46×10^8 kgce in 2016 (BMBS, 2017), indicating that 50% of the household energy use involved on-site CO2 emissions. Therefore, the non-heating fraction ($fr_{nonheat}$) is set to 0.5.

Table 1. Parameters related to anthropogenic heat and CO_2 emissions.

Parameter	Notation	Value	Reference
$C_{M(min)}$	Minimum CO_2 release per capita	120 μmol CO_2 s^{-1} cap^{-1}	Ward et al. (2013)
$C_{M(max)}$	Maximum CO_2 release per capita	280 μmol CO_2 s^{-1} cap^{-1}	Moriwaki and Kanda (2004)
$E_{c,wd}$	Traffic CO_2 EF for weekday	0.207 kg km^{-1} veh^{-1} (4.70×10^6 μmol CO_2 veh^{-1} km^{-1})	Wen et al. (2020, 2022); Zhang et al. (2014)
$E_{c,we}$	Traffic CO_2 EF for weekend	0.209 kg km^{-1} veh^{-1} (4.75×10^6 μmol CO_2 veh^{-1} km^{-1})	Wen et al. (2020, 2022); Zhang et al. (2014)
Tr_{wd}	Mean daily traffic rate for weekday	0.3260 veh km day^{-1} m^{-2}	Yang et al. (2019)
Tr_{we}	Mean daily traffic rate for weekend	0.2664 veh km day^{-1} m^{-2}	Yang et al. (2019)
Fr_{heat}	Fraction of fossil fuels used for heating	0.81	Cui et al. (2019); MHURD (2018); Zhang et al. (2019)
$Fr_{nonheat}$	Fraction of fossil fuels used for energy	0.5	BMBS (2017)
$E_{CO2perJ}$	EF for fuels used in building energy use	0.1688 μmol CO_2 J^{-1}	Cui et al. (2019)
T_{base_HC}	Base temperature for heating degree day	12 °C	this study

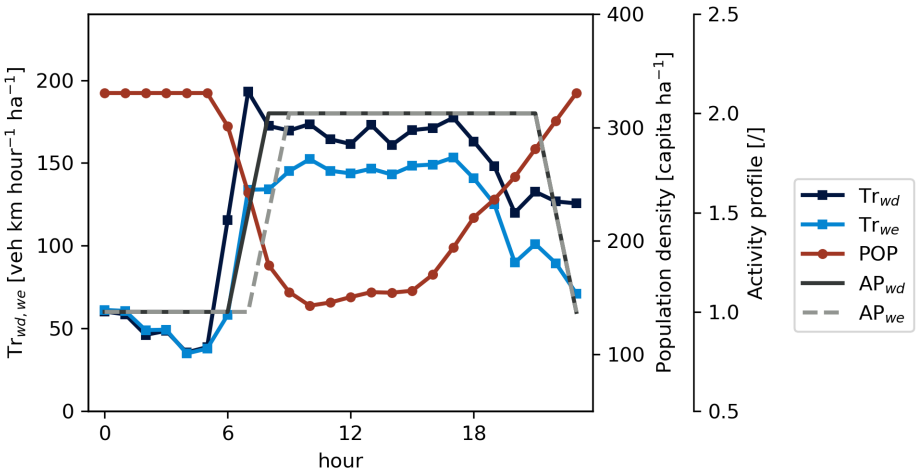

Figure 2. Annual average diurnal cycle of traffic rate for weekday (Tr_{wd}) and weekend (Tr_{we}), population density (POP), and the activity profiles for weekday (AP_{wd}) and weekend (AP_{we}) within the 1 km radius circle around IAP tower.

4.5 Evaluation design

Two different groups of SUEWS runs are made around IAP tower (Fig. 1c). The first run over the years 2009 to 2011 is to evaluate the modelled radiation components against observations. The first 16 months are the spin-up period, and the actual

model evaluation is made from May 2010 to June 2011, when the radiation observations are available. The second SUEWS run from 2015–2016 is to evaluate the turbulent fluxes. The first year is used as a spin-up period and only the year 2016 is used in the evaluation.

The model performance of radiation fluxes is evaluated prior to the simulation of turbulent heat fluxes. The results show that SUEWS is applicable to provide realistic estimates of radiation fluxes in the study area despite the absence of site-specific parameters (Appendix C). The calculation of radiation fluxes is mostly dependent on the land cover fractions under the current scheme adopted by SUEWS (Loridan et al., 2011; Offerle et al., 2003). No visible change in land use type is observed according to satellite images from Google Earth within the modelled area between 2010 and 2016 (figure not shown). Therefore, we assume that the evaluation of radiation fluxes using observations in the years 2011–2012 holds true in 2016.

4.5.1 Sensitivity to vegetation-related parameters

In order to test the model's sensitivity of radiation and turbulent fluxes to vegetation-related parameters, four model cases are designed as follows:

1. Case **base**: control run where model parameters are considered "default" following Kokkonen et al. (2019) (Table S2–S4). The exceptions are: (1) parameters in the environmental response functions (Eq.4 –7) of surface conductance which follow those by Havu et al. (2022a) (Table 2), because the product of response functions calculated following Kokkonen et al. (2019) is too low (95^{th} percentile = 0.19) to obtain realistic estimate of photosynthetic rate; (2) biogenic parameters for Eq.14–15 and soil properties which were updated following Havu et al. (2022a) (Table 2). In addition, $F_{pho,max}$ for grass/lawn (5.5 μmol m^{-2} s^{-1}) is obtained from EC observations of CO_2 flux made over urban lawn in Helsinki in summer 2021 by fitting the conductance parameters ($F_{pho,max,grass}$, $G_2 - G_6$) to the observations following Järvi et al. (2019) (Appendix D).

2. Case **LAI**: Same as case **base** but the parameters for Eq.1 describing the annual behaviour of LAI are optimized using remotely-sensed LAI and CMA-ES (Appendix A). The new optimized LAI parameters are compared with case **base** in Table 3.

3. Case **gs**: Same as case **base** but with g_{max} values collected from observational studies over vegetation species in Beijing (Appendix E). The site-specific g_{max} are in general lower than the values used by case **base** (Table 4).

4. Case **gs_LAI**: Same as case **base**, but with both LAI and g_{max} modified as described in case **LAI** and case **gs**.

Table 2. SUEWS biogenic model parameters used for all case runs in this study.

Parameter	Evergreen/deciduous tree	Grass/lawn	Reference
$\mathrm{LAI}_{i,max}$ ($\mathrm{m^2\ m^{-2}}$)	5.1[a]/5.5[b]	5.9	Järvi et al. (2011)
$\mathrm{LAI}_{i,min}$ ($\mathrm{m^2\ m^{-2}}$)	4.0[a]/1.0[b]	1.6	Järvi et al. (2011)
$F_{pho,max,i}$ (μmol $\mathrm{m^{-2}\ s^{-1}}$)	8.4[c]	5.5[d]	[c]Havu et al. (2022a); [d]this study
G_1	3.5	3.5	Havu et al. (2022a)
G_2	477	477	Havu et al. (2022a)
G_3	0.66	0.66	Havu et al. (2022a)
G_4	0.89	0.89	Havu et al. (2022a)
G_5	30	30	Havu et al. (2022a)
G_6	0.36	0.36	Havu et al. (2022a)
$\Delta\theta_{WP}$ (mm)	132	132	Havu et al. (2022a)
$K_{down,max}$ ($\mathrm{W\ m^{-2}}$)	1200	1200	Järvi et al. (2014)
T_L (°C)	-10	-10	Ward et al. (2016)
T_H (°C)	55	55	Ward et al. (2016)
a_i	0.78[c]	2.1[e]	[c]Havu et al. (2022a); [e]Järvi et al. (2019)
b_i	0.08[c]	0.06[e]	[c]Havu et al. (2022a); [e]Järvi et al. (2019)
Soil depth (mm)	1000[c]	349[f]	[c]Havu et al. (2022a); [f]Kokkonen et al. (2019)

[a] Evergreen tree

[b] Deciduous tree

Table 3. Comparison in leaf area index (LAI) parameters between case **base** and case **LAI/gs_LAI**. All vegetation types (evergreen tree, deciduous tree and grass) use the same LAI parameters within one case. Case **base** values are as in Järvi et al. (2011).

	LAI parameters	
	case **base**	case **LAI/gs_LAI**
$T_{base,GDD}$ (°C)	5	5.7
$T_{base,SDD}$ (°C)	10	22
GDD_{full} (°C)	300	446
SDD_{full} (°C)	-450	-1000
$\omega_{1,GDD}$	0.04	-1.42
$\omega_{2,GDD}$	0.001	0.00258
$\omega_{1,SDD}$	-1.5	2.0
$\omega_{2,SDD}$	0.0015	0.0001

Table 4. Comparison of maximum conductances (g_{max}) between case **base** and case **gs/gs_LAI**. Parameters for case **base** follow Järvi et al. (2011). More details can be found in Appendix E.

	g_{max} (mm s^{-1})	
	case **base**	case **gs/gs_LAI**
Evergreen tree	7.4	1.4
Deciduous tree	11.7	7.0
Grass	40.0	3.7

4.5.2 Sensitivity to radius of modelled area

SUEWS output will be evaluated against EC-measured turbulent fluxes, but the challenge is that the source area of the observations are different to the exact modelling domain. To consider the impact of the chosen modelling domain on model evaluation, we designed three additional model cases where different radius circular areas around IAP tower are considered. The default run is with the 1 km radius circle, but SUEWS is also run within 500 m, 750 m, and 1500 m circular areas, corresponding to the flux footprint of roughly 60%, 70%, and 80–90%, respectively (Liu et al., 2012). Used vegetation parameters are as in case **gs_LAI**, but land surface fractions, population, and traffic parameters are modified accordingly (Appendix F).

4.6 Statistical metrics for model evaluation

Common statistical metrics are used to quantify the model performance, including, coefficient of determination (R^2), root-mean-square error (RMSE) and mean bias error (MBE). Simple linear regression is used to estimate the relationship between the model output and the observations, and the square of the correlation coefficient is taken as R^2. The other statistical metrics are defined as follows:

$$\mathrm{RMSE} = \sqrt{\frac{\sum_{i=1}^{n}(y_i - \hat{y_i})^2}{n}}, \mathrm{and} \tag{18}$$

$$\mathrm{MBE} = \frac{1}{n}\sum_{i=1}^{n}(\hat{y_i} - y_i), \tag{19}$$

where $\hat{y_i}$ is the modelled and y_i the measured value. Statistical metrics are calculated at annual and seasonal scale, i.e., DJF (winter), MAM (spring), JJA (summer), SON (autumn).

5 Results and Discussion

5.1 Seasonal dynamics of the optimized LAI

The control case **base** simulates the onset of leaf growth and the ending of senescence reasonably well (Fig. 3). The performance of LAI modelling is further improved after the optimization (Appendix A). In case **base**, the modelled LAI starts to increase rapidly from day of year (DOY) 70 and plateaus at DOY 105, which is too early when compared to the remotely sensed LAI (Landsat 7 LAI). The optimized LAI starts to grow at the same time but slightly slower and peaks 20 days later than **base**. In autumn, LAI modelled by case base drops rapidly at DOY 310, while the optimized LAI starts to decline rapidly at DOY 267. LAI model with the optimized parameters is better at capturing the behavior of senescence than in the control case **base**.

Although previous studies suggested that LAI was generally modelled well using default parameters following Järvi et al. (2011), Ward et al. (2016) reported that leaf-on is reached too early and suddenly in spring in two UK cities. On the contrary, Ao et al. (2018) showed that the simulated LAI might be lower than reality when vegetation remained green in winter and spring in Shanghai, China. These lead to the bias in g_s and therefore Q_E estimates (Eq. 2–3). In Beijing, the rainy season lasts from May to October, while the other time of the year is the dry season (Liu et al., 2012). It is possible that the distinct dry season leads to a lack of soil moisture in spring and autumn and thus influences the LAI seasonal dynamics if there is no external water input (Omidvar et al., 2022). However, the urban green spaces in Beijing are usually sufficiently or even excessively irrigated (Zhang et al., 2017). Observations also provided evidence to support the relationship between air temperature and phenological dynamics in the urban environment in Beijing (Lu et al., 2006; Luo et al., 2007). Therefore, the air temperature-dependent LAI model is applicable in Beijing, but the "default" LAI parameters might be not suitable. We recommend evaluating the LAI model when SUEWS is applied to a different city, and deriving the optimal LAI parameters if necessary.

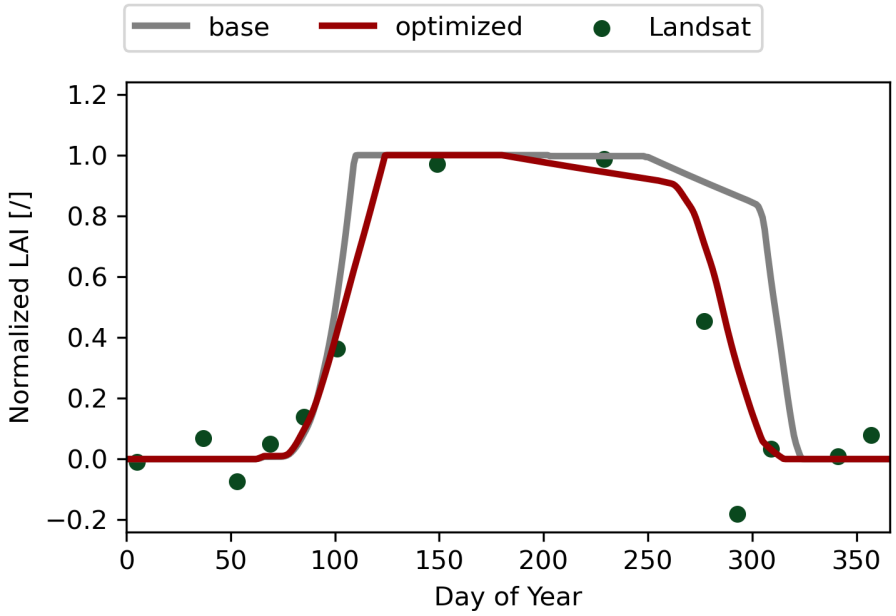

Figure 3. Normalized LAI in 2016, where the value 0 (1) represents the minimum (maximum) of LAI. “Base” denotes the modelled LAI for case **base**, “Landsat” the remotely sensed LAI of the adjacent park near IAP tower, and “optimized” the modelled LAI using the parameters derived with CMA-ES (Appendix A).

5.2 Evaluation of turbulent heat fluxes modelling

Both observed Q_E and Q_H reach their maxima around noon (Fig. 4). The observed Q_E has the largest amplitude during the summer months, while Q_H during the spring months. All four model cases capture their diurnal cycles, but large differences in the amplitude and model performance are observed among the model cases (Fig. 5).

In case **base**, the model overestimates Q_E (with MBE from -7.4 to 48.6 W m^{-2}) except in winter months (Fig. 5). With the optimized LAI (case **LAI**), model performance in Q_E remains virtually unchanged, with RMSE (12.1–94.1 W m^{-2}) and R^2 (0.17–0.53) when compared to case **base** (with RMSE 11.7–96.1 W m^{-2} and R^2 0.20–0.51) (Fig. 5 a–c). Q_E is to a large extent determined by surface conductance which is scaled by g_{max} of each vegetated surface for the modelled area (Eq. 3). Clear improvement is observed when the local g_{max} is used (case **gs**), especially during summer. The overestimation of Q_E is largely reduced, RMSE drops to 11.3–54.7 W m^{-2}, and R^2 increases to 0.25–0.61. With both the optimized LAI and the local g_{max} introduced (case **gs_LAI**), the R^2 is similar to case **gs**, while RMSE slightly decreases by 1–2 W m^{-2} in spring and summer compared to case **gs**. Q_E is underestimated throughout the day in winter (MBE = -8.3 W m^{-2}). Observational studies have shown that combustion-derived water vapor often contributes 5–10% of total urban humidity during heating season (Fiorella et al., 2018; Liu et al., 2022; Salmon et al., 2017). The observed Q_E ranges from 0 to 30 W m^{-2} in winter when vegetation is dormant; this suggests that combustion and evaporation, as the dominant sources of Q_E, might lead to Q_E at this magnitude. The anthropogenic water vapor release might be underestimated by SUEWS in winter.

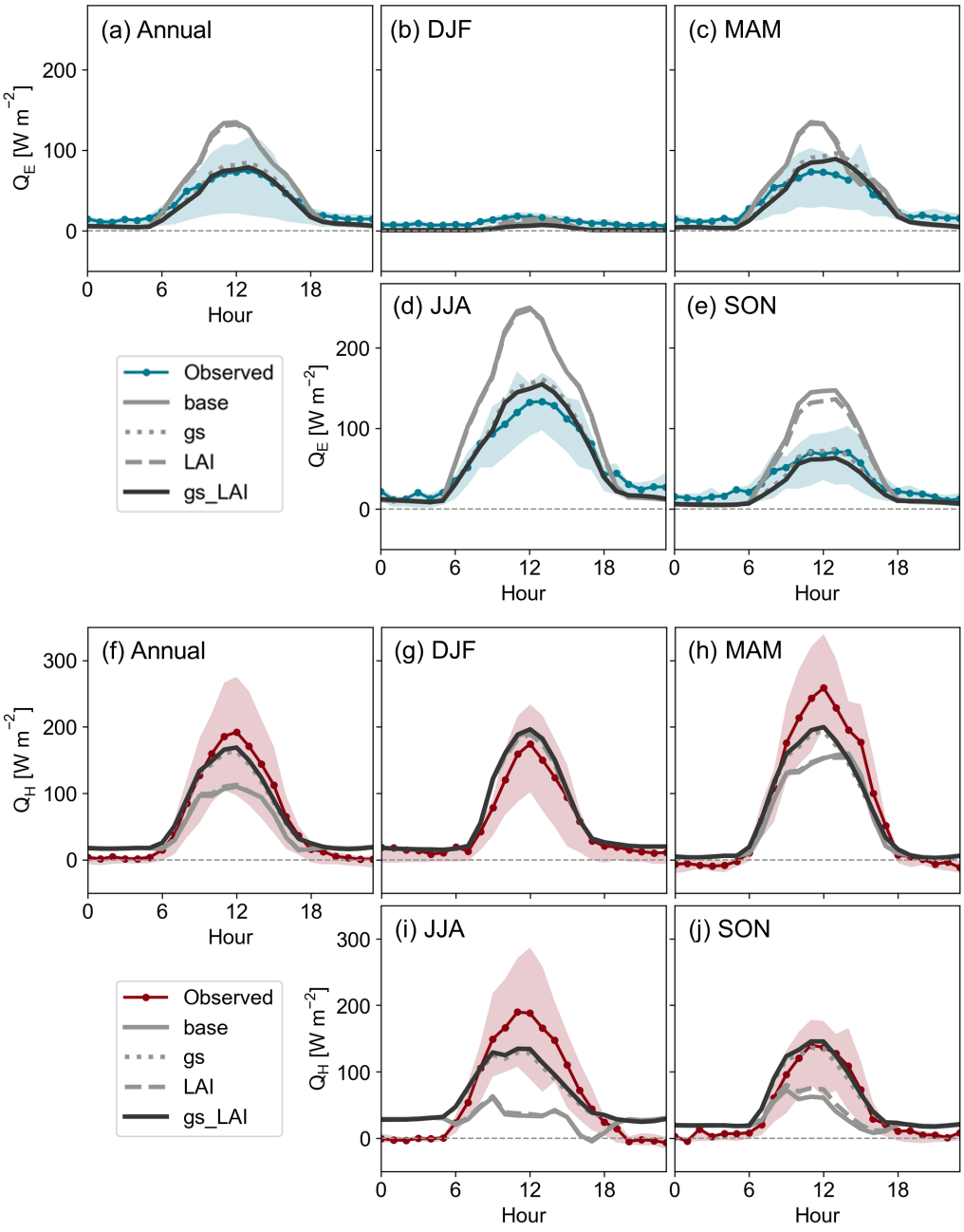

Figure 4. Annual and seasonal mean diurnal cycles of observed and modelled (a–e) latent heat flux (Q_E) and (f–j) sensible heat flux (Q_H) for the four model cases (case **base**, **gs**, **LAI**, and **gs_LAI**) in the year 2016. The shaded area denotes the interquartile range.

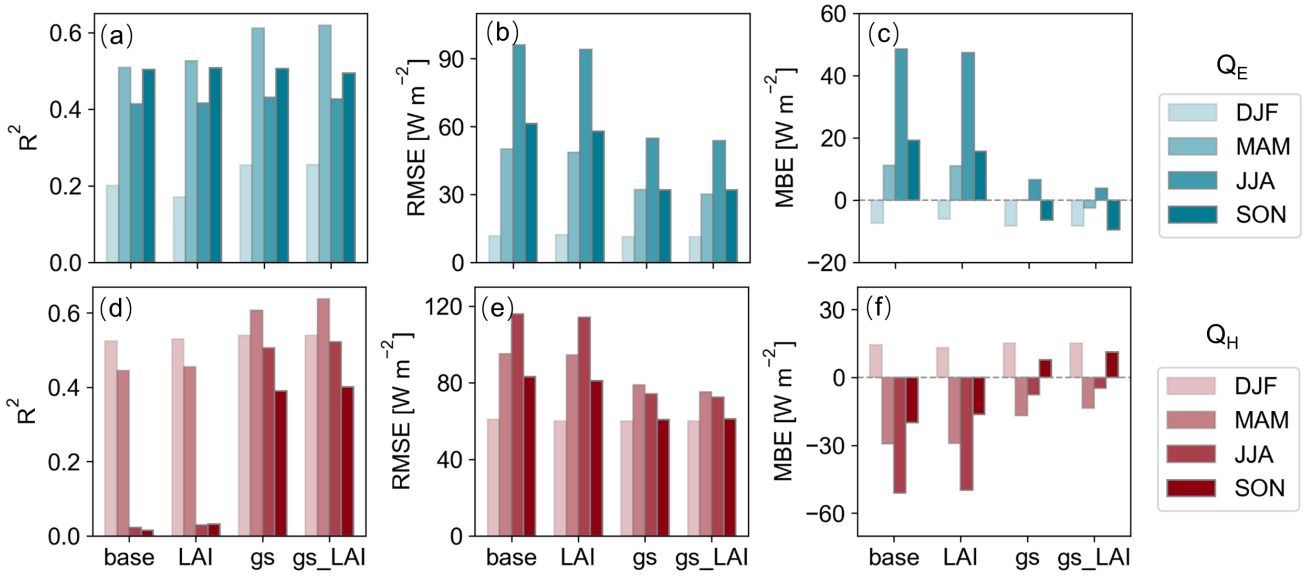

Figure 5. Model performance statistics R^2, RMSE and MBE of (a–c) latent heat flux (Q_E) and (d–f) sensible heat flux (Q_H) for the four model cases (case **base**, **gs**, **LAI**, and **gs_LAI**) in the year 2016.

In SUEWS, Q_H is estimated as the residual of energy balance, and is therefore directly affected by the modelled Q_E. As a result of overestimating Q_E in case **base**, Q_H is greatly underestimated with MBE -51.1–14.4 W m^{-2} and RMSE 60.9–116.0 W m^{-2}. R^2 in summer months and autumn months are lower than 0.1. The model performance is barely improved by the optimized LAI (case **LAI**) but it is noticeably improved after the local g_{max} is introduced (case **gs**) (Fig. 5 d–f). The best model performance for Q_H is obtained by case **gs_LAI**, decreasing the magnitudes of MBE to -13.6–15.2 W m^{-2} and RMSE to 60.1–75.3 W m^{-2}, and increasing R^2 to 0.40–0.64 (Fig. 5 d–e).

Q_H is also influenced by Q_F. Nighttime Q_F in summer might be overestimated, leading to the overestimation in Q_H. Turbulent heat fluxes are also related to ΔQ_S. Both Q_E and Q_H correlate with ΔQs negatively (Eq. 2, Eq. 9). For instance, Q_E is underestimated while Q_H is overestimated at noon in summer in case **gs_LAI**. The decrease in ΔQ_S will lead to a simultaneous increase in Q_E and Q_H, lowering Q_H's bias while increasing Q_E's. Therefore, the adjustment of ΔQ_S can hardly improve the Q_E and Q_H modelling at the same time.

Our results suggest that the model performance of heat fluxes is more sensitive to the adjustment of g_{max} than to the change of LAI seasonal dynamics. By incorporating local LAI and g_{max}, SUEWS simulates the heat fluxes noticeably better, increasing R^2 by 0.03 (0.30) and decreasing RMSE by 27.0 (23.7) W m^{-2} for Q_E (Q_H) compared to case **base**.

5.3 Evaluation of CO_2 fluxes modelling

5.3.1 Model performance

SUEWS basically reproduces the average annual and seasonal diurnal cycle of observed F_C (Fig. 6). The diurnal behaviour is dominated by on-road traffic emission, which reaches 22.6 and 23.0 μmol m^{-2} s^{-1} for the morning peak and afternoon peak, respectively, during the rush hours (Fig. 7). Human metabolism (maximum 4.8 μmol m^{-2} s^{-1}) is the second largest source of CO_2 emissions. In winter, the building CO_2 emission has a maximum of 6.7 μmol m^{-2} s^{-1} in the daytime. The maximum photosynthesis rate is 5.9 μmol m^{-2} s^{-1} around noon in summer, while soil and vegetation respiration constantly serves as a CO_2 source with a rate lower than 3.6 μmol m^{-2} s^{-1}.

Each of the model performance statistics of F_C is of a similar magnitude among cases, indicating the F_C modelling is far less sensitive to the choices of g_{max} and LAI-related parameters than Q_E and Q_H shown in Sect. 5.2 (Fig. 8). Under the current parameterizations, F_{res} considers only air temperature (Eq. 15). The adjustments of g_{max} and LAI parameters affect the modelled heat fluxes, influencing 2 m air temperature, and finally F_{res}, but the difference in annual CO_2 release from respiration is less than 0.01 kg C m^{-2} yr^{-1} among cases. F_{pho} is sensitive to the adjustments of g_{max} and LAI parameters. In case **base**, the large values of g_{max} allow relatively high evapotranspiration (namely Q_E). As a result, the average $\Delta\theta$ during January and June is larger than 105 mm, which is only 27 mm lower than the wilting point deficit ($\Delta\theta_{WP}$). The dry soil lowers the surface conductance and photosynthetic CO_2 uptake through the limiting function of $g(\Delta\theta)$ (Eq. 8). As the local g_{max} is introduced, the soil remains moister with $\Delta\theta$ lower than 75 mm throughout the year, allowing a more favourable condition for the photosynthetic CO_2 assimilation. The CO_2 assimilated through photosynthesis is 0.57 kg C m^{-2} yr^{-1} in case **gs**, which is 0.21 kg C m^{-2} yr^{-1} higher than in case base. The LAI reduction in spring and autumn in case **gs_LAI**, on the other hand, directly limits surface conductance and photosynthesis (Eq. 14), leading to a decrease by 0.07 kg C m^{-2} yr^{-1} in annual photosynthetic CO_2 uptake when compared to case **gs**.

In SUEWS, photosynthetic and respiration rates are proportional to the fractions of vegetated surfaces, which account for only 29% of the modelled area. The magnitude of F_{pho} is substantially lower than the traffic emission, making the effect of photosynthesis, as well as its response to the adjustments of g_{max} and LAI parameters, hardly visible in the F_C diurnal cycles (Fig. 6).

Expectedly, SUEWS has difficulty in capturing the hourly variability of F_C, resulting in the overall low R^2 (0.16–0.22) and high RMSE (12.9–16.4 μmol m^{-2} s^{-1}) (Fig. 8 a). On one hand, observed F_C has great variability at hourly scale throughout the year indicated by the large interquartile range (Fig. 6). On the other hand, under the current parameterization, two of the anthropogenic F_C components are static: modelled traffic emission diurnal cycle is only dependent on whether it is weekend or weekday, and modelled human metabolism diurnal cycle is invariable throughout the year (Fig. 7), making it difficult to capture the extreme values. Other urban F_C bottom-up modelling studies also reported similar challenges in modelling F_C hourly variability in Helsinki and in Basel (Järvi et al., 2019; Stagakis et al., 2022).

SUEWS gives a reasonable estimate of annual accumulated F_C (8.6 kg C m^{-2} yr^{-1}), which is 15% higher than the observed gap-filled value (7.5 kg C m^{-2} yr^{-1}). F_C is overestimated in all seasons, with the lowest MBE (0.2 μmol m^{-2} s^{-1}) in winter and the highest MBE (5.7 μmol m^{-2} s^{-1}) in summer (Fig. 8 c).

There are multiple reasons to explain the difficulty in accurately capturing the diurnal cycle of the observed F_C for each season. First, the underlying seasonal variation in the diurnal wind pattern makes the F_C diurnal cycle from the NW quadrant more "seen" in winter and spring, while the diurnal cycle from SE more "seen" in summer and autumn (Fig. S2 a–d). Second, the observed F_C varies noticeably with wind direction (Fig. S2 e–h). An evident afternoon and evening F_C peak is observed from NE and SE throughout the year. This might be attributed to the relatively high traffic volumes and more severe traffic congestion in the afternoon and evening than in the morning, especially at the nearby crossroads (Fig. 1 d). The morning F_C peak comes from only NE and NW, and only during winter months, suggesting that there might be seasonal variation in the traffic pattern that is not captured by SUEWS. The noticeable increase in F_C in winter from the SE and NW indicates that the building heating emissions might originate mainly from these two sectors. However, SUEWS cannot consider this F_C's wind-direction dependency as it simulates the overall flux from the simulation domain.

Apart from the wind direction, atmospheric stability influences the real-time footprint fetch of F_C (Crawford and Christen, 2015), but this is not considered in our study. Furthermore, there might be biases in simulating the seasonal cycles of F_C components. SUEWS might underestimate the vegetation photosynthetic rate or overestimate the CO_2 release from respiration due to the lack of site-specific biogenic parameters. Nonetheless, the model performance over the F_C diurnal cycle is reasonably good as compared to a previous study (Järvi et al., 2019).

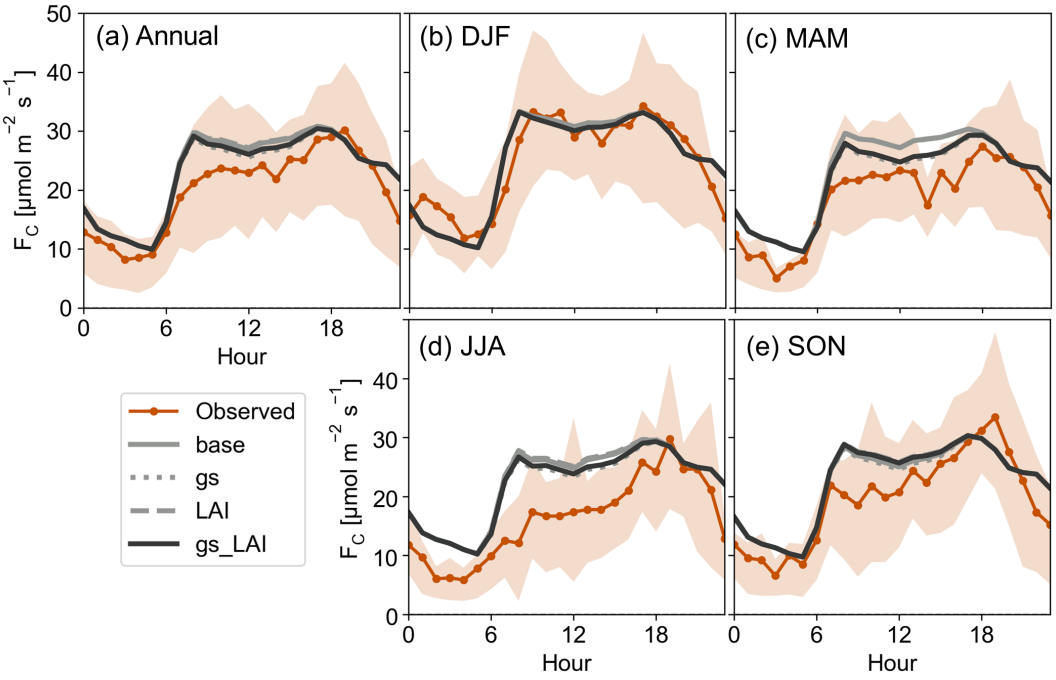

Figure 6. Annual and seasonal average diurnal cycles of observed and modelled CO_2 flux (F_C) for the four model cases (case **base**, **gs**, **LAI**, and **gs_LAI**) in the year 2016. The shaded area denotes the interquartile range.

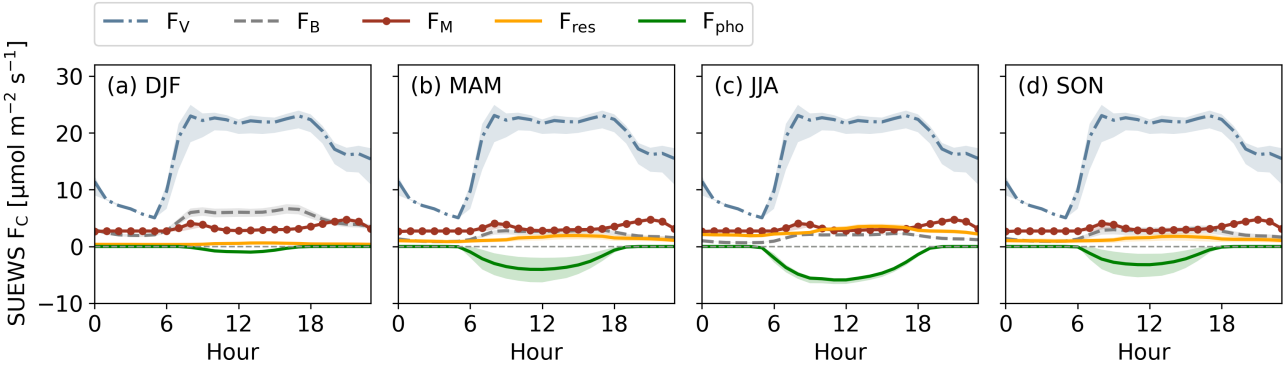

Figure 7. Seasonal average diurnal cycles of modelled CO_2 flux (F_C) components by case **gs_LAI** in 2016. F_V denotes the CO_2 emissions from on-road traffic, F_B buildings, F_M human metabolism, F_{res} vegetation and soil respiration, and F_{pho} the CO_2 uptake by vegetation photosynthesis. Positive values indicate the emissions of CO_2 and negative values indicate the uptake of CO_2 with respect to the atmosphere. The shaded area denotes the interquartile range.

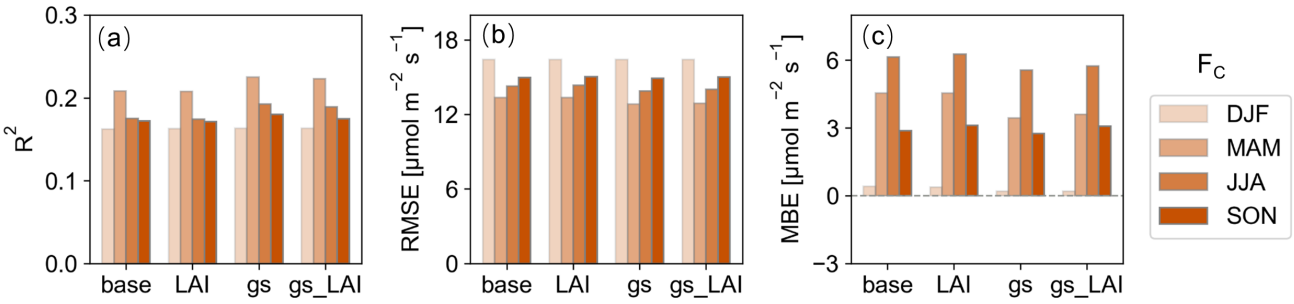

Figure 8. Model performance statistics (a) R^2, (b) RMSE and (c) MBE of CO_2 flux (F_C) for the four cases (**base**, **gs**, **LAI**, and **gs_LAI**) in the year 2016.

Uncertainties in traffic emission originate from the traffic rates and EFs. SUEWS adopts static traffic EFs, and neglects the relationship between traffic emission and T_{air} as reported by Alvarez and Weilenmann (2012) and Fontaras et al. (2017). In order to examine the impact of seasonal variation of T_{air} in traffic emission, correction is conducted using the regression function following Zhang et al. (2021), but only a marginal difference is seen at monthly scale: a difference of 3% in winter, -2% in spring, ~0% in summer and -1% in autumn. Therefore, we believe that the static traffic EFs adopted by SUEWS can provide reasonable traffic emission without considering the seasonal dynamics of T_{air}.

Järvi et al. (2019) reported that using a different coefficient of CO_2 release per capita (C_M) lead to a 6% decrease in human metabolic CO_2 emission estimate. If C_M is set to a daily mean value of 242 μmol m^{-2} s^{-1} (Prairie and Duarte, 2007) instead of the current values (Table 1), the human metabolic emission will increase and the annual F_C will be 4% higher than the original estimate.

Building emissions are calculated based on the Q_F estimates and heating fraction. Modelled average Q_F in December is 52.7 W m^{-2}, which is higher than another model estimate (21.6 W m^{-2}) in the modelled area (Wang et al., 2020). Observations of Q_F are rarely available, and thus these Q_F estimates have not yet been validated. The representativeness of the heating fraction estimated from yearbook statistics is yet to be examined because the location and heating capacity of heating boilers within the modelled area is unknown. However, the building emission estimate (0.97 kg C m^{-2} yr^{-1}) falls in the range of estimates (~0–3.0 kg C m^{-2} yr^{-1}) by other cities (Björkegren and Grimmond, 2018; Christen et al., 2011; Järvi et al., 2019; Moriwaki and Kanda, 2004).

The modelled CO_2 release by respiration is larger than CO_2 assimilated through photosynthesis in our study. At the annual scale, urban vegetative surfaces can have a net CO_2 uptake (Awal et al., 2010; Konopka et al., 2021), but may also have a net emission (Peters and McFadden, 2012). Admittedly, bias might exist in biogenic CO_2 flux estimates since the parameters used in this study are derived from the observations over street trees in Helsinki and over a lawn at Ossinlampi, Finland, where the climate and vegetative species are different from Beijing. With these parameters, the model might underestimate the CO_2 sequestrated by the local vegetation, or overestimate the CO_2 release by respiration.

5.3.2 The impact of the modelling domain size

The surroundings of IAP tower are heterogeneous in terms of land surface fraction and mean daily traffic rate (Fig. 9 a). The fraction of vegetated surfaces is higher closer to the tower than further away due to the green spaces adjoining IAP tower (Fig. 1 b). Additionally, there is a traffic hot spot on the 3rd Ring North Road located 850 m to the south of IAP tower (Fig. 1 d), where the traffic rate is 2 to 7 times the value for the other roads inside the circle of a 1000 m radius (figure not shown). A large increase of 26% in daily traffic rate is seen when the radius of modelling domain is 1000 m or 1500 m when compared to domains with lower radii (Fig. 9 a). Thus, the modelled annual accumulated F_C largely depends on the modelling domain size chosen, giving estimates of 7.4, 7.6, 8.6 and 8.7 kg C m^{-2} yr^{-1} for the radii of 500 m, 750 m, 1000 m, and 1500 m, respectively. Observational annual F_C (7.5 kg C m^{-2} yr^{-1}) falls within this range, which indicates the good model performance of SUEWS (Fig. 9 b).

The turbulent flux modelling is usually evaluated over a fixed extent such as a circle with a certain radius to approximate the flux source area (Demuzere et al., 2017; Järvi et al., 2019). However, when a circle with the radius $\geq$ 1000 m is selected to approximate the $\geq$80% footprint fetch in our study, SUEWS does not give the closest estimate of annual F_C. This can be explained by the mismatch between the modelling domain and the real flux source area—the single fixed-extent modelled area cannot perfectly represent the land surface characteristics (e.g., the nonuniform land cover and human activities), biasing turbulent flux modelling (Chu et al., 2021; Laine et al., 2009). First, the accumulated footprint area of the observed fluxes is irregular in shape and vary with time (Liu et al., 2012). Second, the relative contribution to flux from the land surface decreases as the distance to the measurement instrument increases (Christen et al., 2011; Rebmann et al., 2005). Thus, when the modelling domain is a 1000 m radius circle, the model might underestimate the relative contribution from the adjacent vegetated surface, and overestimate the contribution of the traffic hot spot at the edge of 80% footprint fetch.

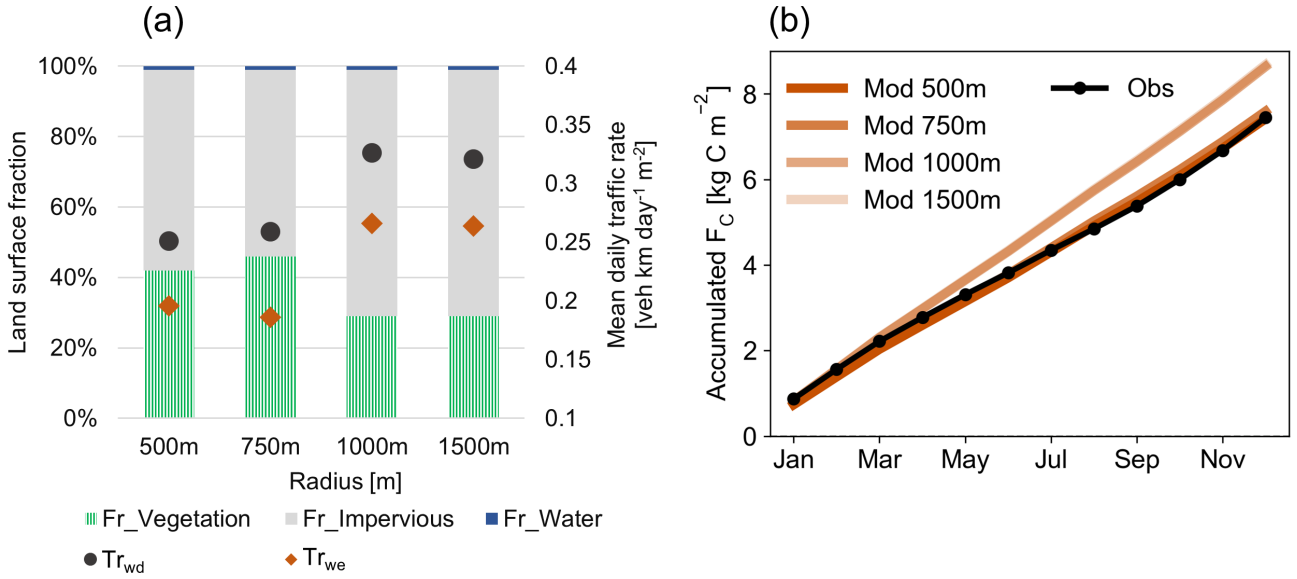

Figure 9. (a) Land use fraction and mean daily traffic rate ($Tr_{wd/we}$), and (b) accumulated CO_2 flux (F_C) for modelling domain with the radius ranging from 500 m to 1500 m. "Wd" denotes weekday, "we" weekend; "Mod" denotes modelled F_C, and "Obs" observed F_C. Note that in (b) the lines for Mod 500m and Mod 750 m nearly overlap, and the lines for Mod 1000m and Mod 1500m nearly overlap.

Regardless of the modelling domain size, traffic is the dominant CO_2 source, contributing 59–70% to the total CO_2 emissions, followed by human metabolism (14–18%), building energy use (11–14%), and CO_2 release by vegetation and soil respiration (6–10%). Vegetation photosynthesis offsets only 5–10% of the total annual CO_2 emissions (Fig. 10). Several bottom-up modelling studies show that the on-road traffic is the greatest source in a densely built neighbourhood, contributing to 70% in central London, 61% in Helsinki, 53%–78% in Tokyo, 70% in Vancouver, while human metabolism also plays an important role, contributing 5–39% to the annual total F_C (Björkegren and Grimmond, 2018; Christen et al., 2011; Järvi et al., 2019; Moriwaki and Kanda, 2004). Our results are in general agreement with these studies. The contribution of the local building emissions within the study area is more variable among cities: a contribution of 70% is reported in Basel (Stagakis et al., 2022), while ~0% in Helsinki (Järvi et al., 2019), and our estimate falls in this range. The direct CO_2 sequestration by urban plants is minor compared with the total CO_2 emissions in this densely built neighbourhood, which is in general agreement with Pataki et al. (2011) and Christen et al. (2011). For more accurate biogenic component estimates in Beijing, photosynthetic and respiration observations over local species are needed in the future.

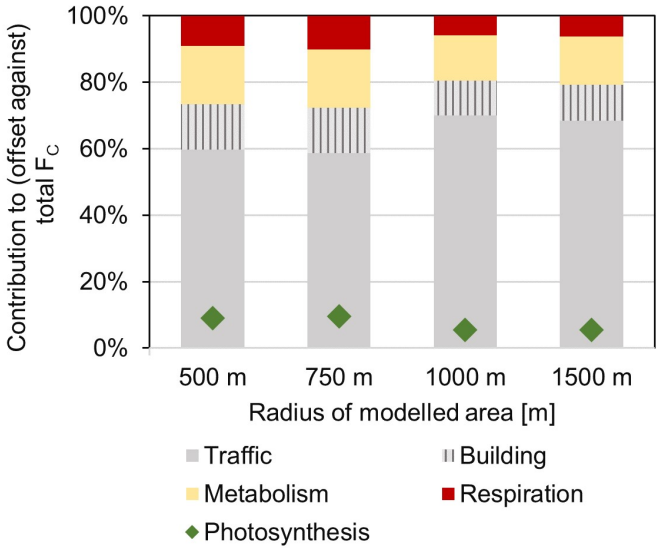

Figure 10. The contribution to total CO_2 emissions by each component at the annual scale for the modelled area with a radius ranging from 500 m to 1500 m. Note that for photosynthesis the percentages denote the offset against total CO_2 emissions.

6 Conclusions

A correct description of vegetation is vital in order to simulate the energy and CO_2 fluxes over urban surfaces using the urban land surface model SUEWS. In this study, the impact of selecting appropriate vegetation parameters, including LAI parameters and g_{max}, on simulating the surface fluxes is examined in Beijing, China. Besides, the newly-developed CO_2 emissions module in SUEWS is evaluated against EC measurements.

The model performance of heat fluxes (Q_E and Q_H) is more sensitive to the adjustment of g_{max} than to the change of LAI seasonal dynamics in our study area. The LAI model has been improved by using CMA-ES to optimize the LAI parameters with a remotely sensed LAI product, providing more realistic vegetation phenological dynamics, especially for the senescence season. The parameter g_{max} was parameterized according to leaf-level observations of vegetation species in Beijing. By incorporating local LAI and g_{max}, SUEWS simulates the heat fluxes noticeably better, increasing R^2 by 0.03 (0.30) and decreasing RMSE by 27.0 (23.7) W m^{-2} for Q_E (Q_H), and showing more realistic seasonal dynamics when compared to EC observations.

F_C modelling appears to be less sensitive to the choices of LAI-related parameters and g_{max}. Only one of the F_C components, F_{pho}, responds noticeably to them. SUEWS can catch the general diurnal and seasonal behaviour of F_C but tends to overestimate F_C, especially over summer months. We also tested the influence of chosen modelling domain size on simulated F_C. By selecting the modelled radii of circular area ranging from 500 m to 1500 m (i.e., accumulated footprint area from 60% to 80–90%), the modelled annual F_C ranges from 7.4 to 8.7 kg C m^{-2} yr^{-1}, which is comparable with the EC observations (7.5 kg C m^{-2} yr^{-1}). This shows that the model performs well also on the annual scale. Regardless of the modelling domain size, traffic is the dominant CO_2 source, contributing 59–70% to the total CO_2 emissions, followed by human metabolism

(14–18%), buildings (11–14%), and CO_2 release by vegetation and soil respiration (6–10%). Vegetation photosynthesis offsets only 5–10% of the CO_2 emissions.

We highlight the importance of choosing more site-specific LAI parameters or g_{max} when SUEWS is used for heat fluxes modelling before the more advanced application such as urban climate and hydrological modelling. Observations are needed to support more accurate parameterizations of biogenic CO_2 fluxes. We believe that the bottom-up approach to model F_C by SUEWS can be a promising tool in capturing the CO_2 emission hot spots, quantifying the relative contribution of the local CO_2 sources, and assisting to mitigate urban CO_2 emissions.

Appendix A: Workflow of LAI parameters optimization

In SUEWS, LAI influences the surface conductance, and subsequently Q_E and F_{pho} (Sect. 2). A workflow for parameter derivation for the LAI sub-model based on remotely-sensed data is designed for natural ecosystems (Omidvar et al., 2022). However, vegetation in urban areas behaves differently from natural ecosystems (Zhang et al., 2022), and needs to be considered separately. Therefore, we propose a workflow to obtain the parameters for urban area based on remotely-sensed LAI and Covariance matric adaptation evolution strategy (CMA-ES). This workflow can also be applied to natural ecosystems. The related data and codes are openly available (Zheng et al., 2022).

Covariance matric adaptation evolution strategy (CMA-ES) is one of the strategies for numerical optimization of non-convex problems. It is based on the principle of biological evolution. The evolution strategy takes a certain number of individuals (candidate solutions) in a stochastic way, selects individuals based on the fitness, and repeats this process for generations so that a better or an optimal solution is obtained. Adaptation of the covariance matrix amounts to learning a second order model of the underlying objective function. Compared with classic optimization methods, CMA-ES requires neither derivatives nor an objective function; it only requires the ranking of candidate solutions. Besides, CMA-ES outranks many of other optimization algorithms, performing especially strong on "difficult functions" or larger dimensional search spaces (Hansen et al., 2010).

Taking our study area as an example, the LAI parameters are optimized as the following:

1. LAI derivation. A six-year time series (2011–2016) of LAI of the vegetation in an adjacent park near IAP tower is calculated from the atmospherically corrected surface reflectance provided by USGS Landsat 7 Enhanced Thematic Mapper + (ETM+) (30 m spatial resolution) via the Google Earth Engine Data Catalog (Masek et al., 2006). The time series is treated as the “original LAI”.

2. Spikes removal. There are outliers in the LAI time series caused by instrument problems, uncertainties of retrieval algorithm, and cloud contamination. Values larger than 10 m^2 m^{-2} and negative values are first removed. The LAI values during December and January are set to a fixed value, i.e., the average of these months (0.2 m^2 m^{-2}), in order to reduce the noise in winter and improve the optimization performance.

3. Scaling the original LAI to the canopy level. The original LAI might be noticeably lower than the measured LAI at the canopy level over a homogeneous vegetated surface. Nonetheless, the original LAI provides the signals of vegetation

phenology (e.g., leaf-out, peak growing season, leaf-fall). In order to give a more realistic estimate of LAI at the canopy level, the original LAI needs to be scaled. Therefore, LAI_{max} and LAI_{min} need to be given manually, preferably based on observational studies over local species. Here, the original LAI is scaled to allow the optimized LAI to reach 5–6 m^2 m^{-2} in the peak growing season as reported by an observational study in Beijing (Wang et al., 2021). The canopy-level LAI is marked as the "input LAI" for the process of optimization and marked as the "observed LAI" for the process of evaluation.

4. Interpolation. The observed LAI are linearly interpolated between values to obtain a daily time series, marked as the "interpolated LAI".

5. Parameters derivation using CMA-ES. The time series of interpolated LAI and T_{air} are subjected to CMA-ES to optimize the parameters. Using the LAI model and the parameters derived, LAI is calculated and marked as the "predicted LAI".

Despite the spike removal step, noise is observed in the LAI time series such as the abrupt drop and recovery during summer. Smoothing techniques are used to extract valid information from the satellite data with noise. In other words, the overall pattern (e.g., the moving average) of the time series is the information of interest, and CMA-ES has successfully reproduced the overall pattern out of the input LAI time series contaminated by noise (Fig. A1 a). Moreover, the LAI has been "scaled" as shown in step 3 to allow the output LAI to reach 5–6 ^{2} m^{-2} in order to avoid the underestimation of the predicted values. Therefore, the noise in the input LAI during summer is kept since it has little impact on the outcome. We conclude that the model performance is overall good (with R^2 = 0.74 and RMSE = 1.2 m^2 m^{-2}) (Fig. A1 b).

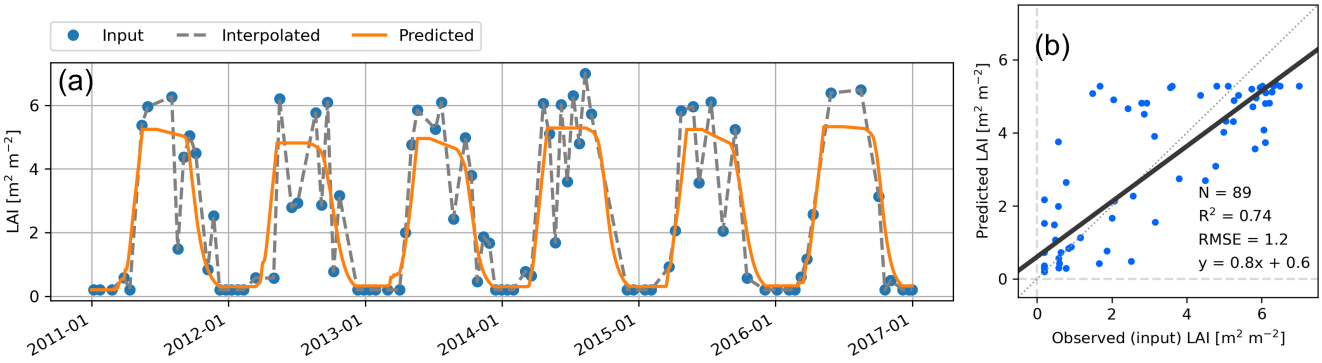

Figure A1. (a) Time series of the the input, the interpolated, and the predicted leaf area index (LAI), and (b) comparison of the predicted against the observed LAI.

Appendix B: Evaluation of WFDE5 reanalysis against observed meteorological variables

To force SUEWS, local scale meteorological data within the inertial sublayer is required. However, they can be unavailable for the area and period desired. Reanalyses provide spatially and temporally complete datasets, which might make the modelling

run easier for users. Kokkonen et al. (2018) and Kokkonen et al. (2019) evaluated one of the reanalyses, WATCH Forcing Data ERA-Interim (WFDEI), suggesting that WFDEI can serve as the forcing of SUEWS, but should be corrected beforehand when the bias is large.

WFDE5 is a bias-corrected dataset of near-surface meteorological variables derived from the fifth generation of the European Centre for Medium-Range Weather Forecasts (ECMWF) atmospheric reanalysis (ERA5) (Cucchi et al., 2021). It is generated using the same methodology as WFDEI, and provides a single layer at 0.5° spatial resolution and hourly temporal resolution. The evaluation of WFDE5 and the use of it as forcing data to SUEWS have been neglected so far. Here, we compare WFDE5 against observed meteorological variables including air temperature (T_{air}), relative humidity (RH), wind velocity (U) at 47 m, and incoming shortwave radiation (K_{down}) at 140 m on IAP tower (Liu et al., 2012). The evaluation of K_{down} is conducted from May 2010 to June 2011, and the rest from January 2010 to December 2011. All the observed variables are resampled from 30-minute to 1-hour resolution.

Table B1. The height of WFDE5 and observed meteorological variables.

	WFDE5	Observations
T_{air}	2 m	47 m
RH	near surface	32 m
U	10 m	47 m
K_{down}	near surface	140 m

With the difference in height for each meteorological variable (Table B1), however, WFDE5 is close to the observed as a whole (Fig. B1). Compared with the observed, WFDE5 T_{air} is lower, RH higher, U lower, and K_{down} higher. WFDE5 may underestimate T_{air}, and overestimate RH, for neglecting the urban anthropogenic heat release; WFDE5 might overestimate K_{down} due to insufficient consideration of aerosol's effect in decreasing solar radiation received by the urban surface. The lower U of WFDE5 can be explained by the lower height compared with the observations (Table B1). If the WFDE5 U is adopted as forcing of SUEWS, aerodynamic resistance might be overestimated, and therefore Q_E underestimated.

Admittedly, some meteorological variables of WFDE5 correlate poorly with the observations in a particular season (e.g., R^2=0.13 for U in JJA). However, the overall high R^2, and low RMSE and MBE in magnitude suggest that WFDE5 provides reasonably good estimates of each meteorological variable (Table B2). Therefore, WFDE5 is adopted as the forcing data of SUEWS in this study.

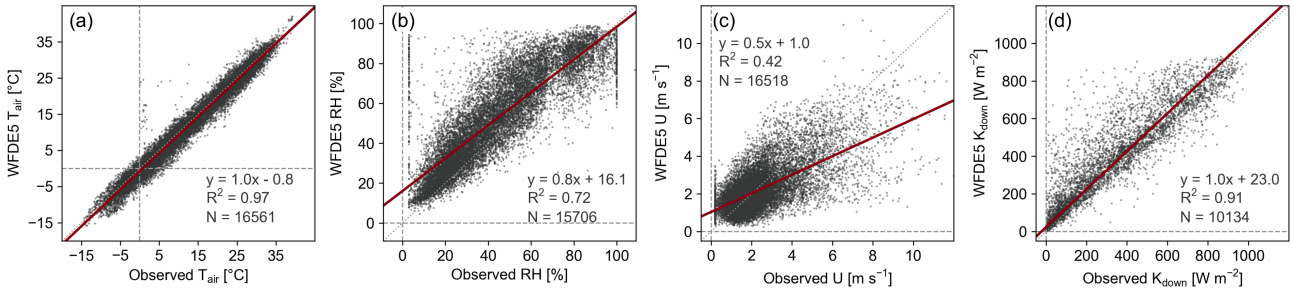

Figure B1. Comparison of WFDE5 and observed meteorological variables including (a) air temperature (T_{air}), (b) relative humidity (RH), (c) wind velocity (U) and (d) incoming solar radiation (K_{down}) at an hourly resolution.

Table B2. Statistics for WFDE5 compared against the observed meteorological variables.

	Season	average		R^2	RMSE	MBE	N
		WFDE5	Observed				
T_{air} (°C)	DJF	-2.1	-1.2	0.83	2.3	-1.0	4217
	MAM	12.7	13.5	0.92	2.5	-1.0	4100
	JJA	26.2	26.8	0.77	2.1	-0.5	3966
	SON	13.8	14.2	0.94	1.9	-0.4	4278
RH (%)	DJF	41.8	32.4	0.77	13.4	9.3	4216
	MAM	41.6	34.1	0.74	13.8	7.9	3986
	JJA	66.6	59.9	0.71	12.6	5.1	3546
	SON	60.2	49.3	0.50	20.6	10.9	3958
U (m s^{-1})	DJF	2.1	2.7	0.52	1.3	-0.5	4217
	MAM	2.7	2.8	0.45	1.4	-0.1	4100
	JJA	1.9	1.9	0.13	1.2	0.1	3949
	SON	2.0	1.9	0.45	1.0	0.0	4252
K_{down} (W m^{-2})	DJF	117.0	99.2	0.94	50.6	19.5	2160
	MAM	222.5	218.1	0.93	82.7	19.7	2941
	JJA	216.4	189.3	0.86	110.5	38.2	2883
	SON	140.9	124.7	0.93	58.9	16.5	2150

Appendix C: Evaluation of radiation fluxes

The radiation parameterization scheme Net All-wave Radiation Parameterization (NARP) does not involve g_{max} or LAI. As expected, the four experiments (Sect. 4.5.1) give identical radiation flux components in the output. Therefore, only the case **gs_LAI** is further analyzed here.

The model performance of SUEWS in simulating radiation fluxes is good (Fig. C1, Table C1) and it can reproduce the diurnal cycle of each radiation flux well (Fig. C2). K_{up} is overestimated in all seasons with MBE ranging from 0 to 10 W m^{-2}. At least partly, this overestimation can be explained by the positive bias (MBE $>$ 15 W m^{-2} in all seasons) of WFDE5 K_{down} when compared to the observed K_{down} (Appendix B). The overestimation in K_{up} can also be caused by surface albedo. Observational studies have shown that the urban surface albedo near IAP tower varies between 0.1 and 0.15 with season (Jiang et al., 2007; Miao et al., 2012). The annual bulk albedo for the modelling domain given to SUEWS is 0.14, which is relatively high but still consistent with the observations. A larger positive bias in K_{up} is observed in summer than in winter. Surface albedo is influenced by many factors such as surface wetness and street canyon trapping effect (Ao et al., 2016; Dou et al., 2019), which have not yet been considered by SUEWS. By simply (1) adjusting the albedos for surface types following Ward et al. (2016), and (2) allowing albedo for vegetation to vary from a lower value in summer to a higher value in winter (Table S5), the RMSE for K_{up} decreases for all seasons, especially in summer (from 18.0 to 13.6 W m^{-2}), but this has only a minor impact on Q_N modelling (Table S6).

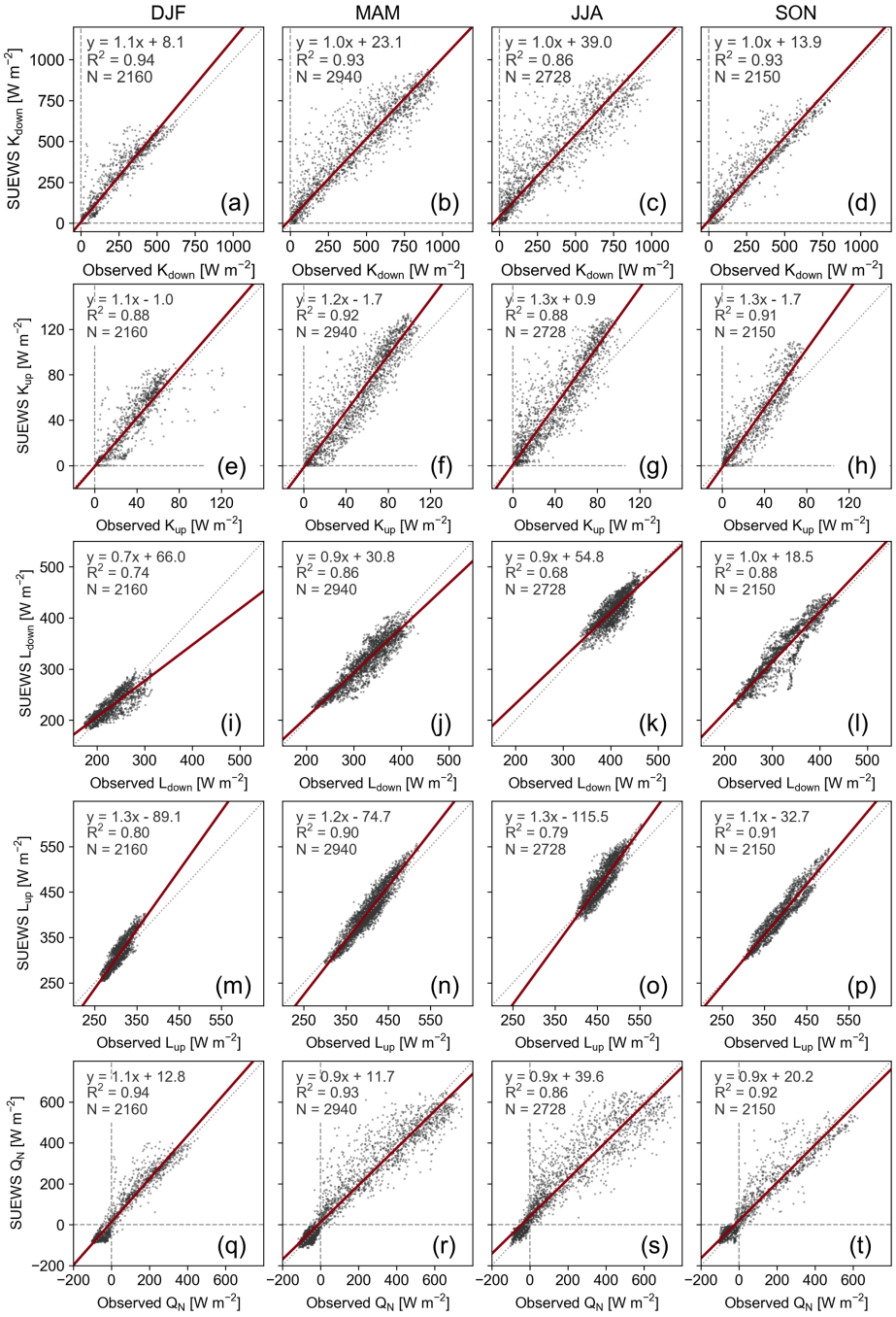

Figure C1. Input or modelled vs. observed hourly radiation fluxes, including (a–d) incoming solar radiation (K_{down}), (e–h) outgoing shortwave radiation (K_{up}), (i–l) incoming longwave radiation (L_{up}), (m–p) outgoing longwave radiation (L_{up}), and (q–t) net radiation (Q_N) from May 2010 to June 2011. Note that only K_{down} is input and the rest are model output.

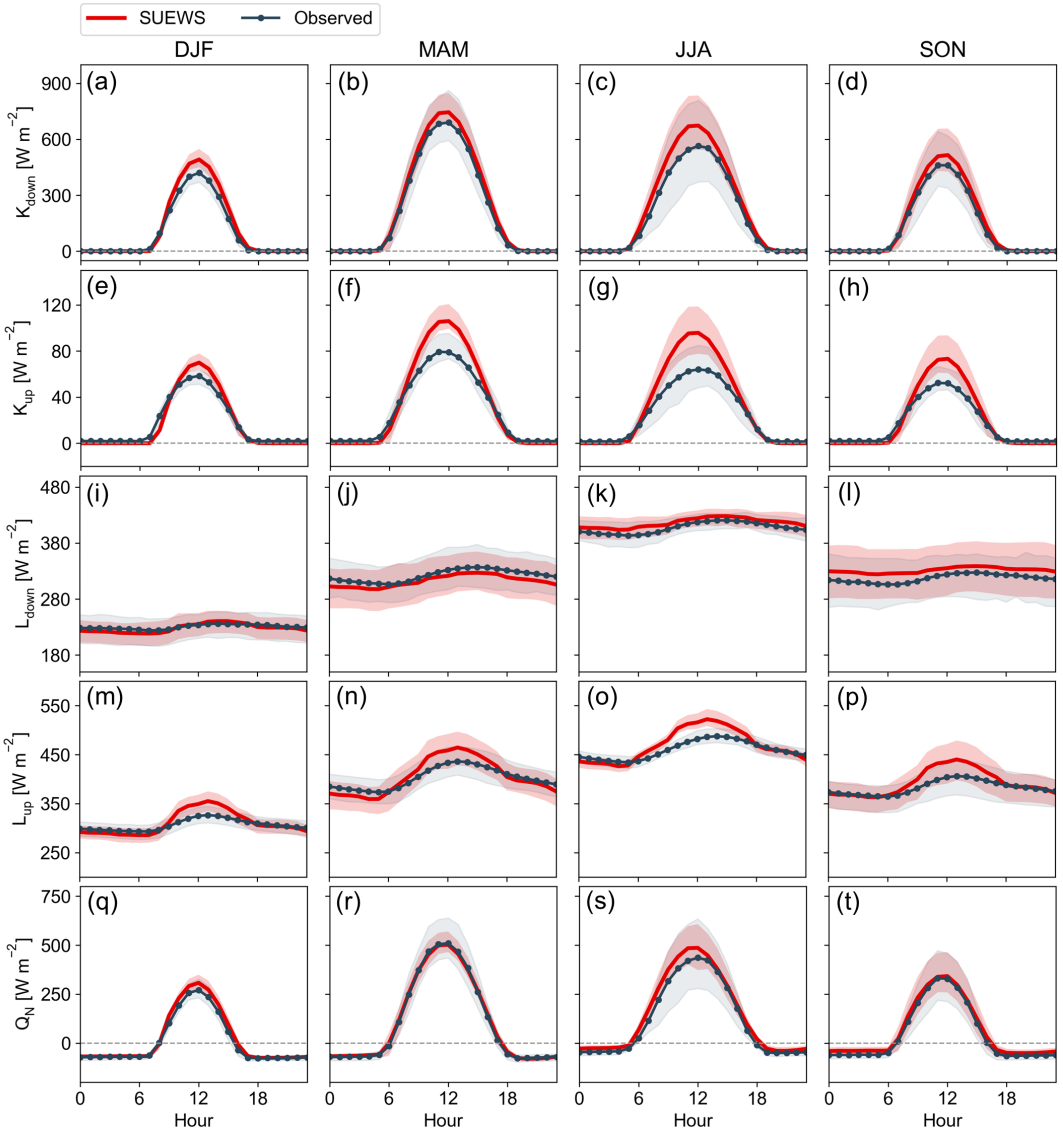

Figure C2. Average diurnal cycle of input or modelled and observed hourly radiation fluxes by season, including (a–d) incoming solar radiation (K_{down}), (e–h) outgoing shortwave radiation (K_{up}), (i–l) incoming longwave radiation (L_{up}), (m–p) outgoing longwave radiation (L_{up}), and (q–t) net radiation (Q_N) from May 2010 to June 2011. Shading area denotes the standard deviation. Note that only K_{down} is input and the rest are model output.

The average seasonal and diurnal cycles of L_{down} are well captured by the model (Fig. C2 i–l), although R^2 (0.68–0.88) is lower than with other radiation fluxes. The difference might result from the discrepancy between the observed and modelled cloud fraction as clear skies and overcast conditions are especially difficult to capture by the radiation model NARP, as reported also by Ao et al. (2016) and Ward et al. (2016). The diurnal amplitude of L_{up} is slightly overestimated by SUEWS (Fig. C2 m–

p). The model tends to overestimate L_{up} particularly at high values of L_{up} (Fig. C1 m–p). The values of emissivity of building materials used in SUEWS might be slightly higher than in reality. L_{up} is also dependent on K_{down} in NARP. Therefore, the overestimation of L_{up} can be partly explained by the overestimated K_{down} provided by WFDE5, especially around noon and in summer.

We conclude that SUEWS is applicable to provide a realistic estimate of radiation fluxes in Beijing, in general accordance with previous studies (Järvi et al., 2014; Karsisto et al., 2016; Ward et al., 2016), despite the absence of site-specific parameters.

Table C1. SUEWS model performance statistics for radiation fluxes. The abbreviations are the same as Fig. C1. Note that K_{down} is an input and others are output of SUEWS.

	Season	R^2	RMSE	MBE	N
K_{down}	DJF	0.94	52.3	19.5	2160
	MAM	0.93	82.6	19.8	2940
	JJA	0.86	110.4	39.3	2728
	SON	0.93	59.6	16.6	2150
K_{up}	DJF	0.88	9.2	0.2	2160
	MAM	0.92	14.8	5.0	2940
	JJA	0.88	18.0	8.1	2728
	SON	0.91	11.6	3.3	2150
L_{down}	DJF	0.74	16.0	-2.4	2160
	MAM	0.86	20.5	-10.0	2940
	JJA	0.68	18.1	8.8	2728
	SON	0.88	23.7	12.9	2150
L_{up}	DJF	0.80	15.3	3.8	2160
	MAM	0.90	18.6	3.2	2940
	JJA	0.79	22.1	10.5	2728
	SON	0.91	18.6	9.2	2150
Q_N	DJF	0.94	38.0	13.2	2160
	MAM	0.93	64.6	1.5	2940
	JJA	0.86	87.0	29.5	2728
	SON	0.92	50.8	17.0	2150

Appendix D: Fitting maximum photosynthetic rate for vegetation type of grass/lawn

In order to find the maximum photosynthetic rate for the vegetation type of grass to be used in SUEWS simulation, the environmental response functions $g(T_{air})$, $g(\Delta q)$, $g(\Delta\theta)$, and $g(K_{down})$ in Eq. 14 were fitted to observations from an eddy covariance (EC) station (60°11'16.02"N, 24°49'56.85"E) situated in an urban lawn in Espoo, Finland. A 1.2 m high EC tower was located at the center of the urban lawn covering an area of 0.7 ha. The EC setup consisted of a three-dimensional sonic anemometer (Metek GmbH, Germany) for measuring the three wind components and sonic temperature, and a closed-path infrared gas analyser (LI-7200; LI-COR, Lincoln, NE, USA) for measuring the CO_2 and H_2O mixing ratios. The gas analyser inlet was positioned 13 cm below the anemometer and air was drawn into the gas analyser using a 60 cm length of steel tube, having an inner diameter of 4.57 mm and a mean flow rate of 12 l min^{-1}. The tube was heated to avoid water vapor condensation on tube walls. The raw EC data were sampled at 10 Hz and stored for post-processing. The steps before 30-min flux calculations consisted of de-spiking, linear de-trending, and planar fitting of the raw data.

The biogenic CO_2 flux $F_{c,bio}$ from EC measurements was partitioned into F_{res} and F_{pho} using the night-time temperature dependency of F_{res}. The nighttime $F_{c,bio}$ was considered as nighttime F_{res}, and it was related to the observed T_{air} by fitting the exponential model:

$$F_{res} = a_{grass} \cdot exp(T_{air} b_{grass}), \tag{D1}$$

where a_{grass} and b_{grass} are parameters controlling the temperature dependency. The nighttime temperature dependency of F_{res} was then extrapolated to daytime, and F_{pho} was then calculated by

$$F_{pho} = F_{C,bio} - F_{res}. \tag{D2}$$

Then F_{pho} was used as a dependent variable, whereas on-site measurements of net radiation (CNR4; Kipp&Zonen, Delft, Netherlands), air temperature, and relative humidity (HMP110 A15; Vaisala Oyj, Vantaa, Finland) and soil moisture (ML3 Thetaprobe; Delta-T, Cambridge, UK) were used to estimate the independent variables in $g(T_{air})$, $g(\Delta q)$, $g(\Delta\theta)$ and $g(K_{down})$. Atmospheric pressure from Finnish Meteorological Institute Kumpula station was used to calculate Δq. Additional reference values of soil properties (field capacity and wilting point), which were estimated to be same as in an urban lawn in Kumpula (Järvi et al., 2019), were used to calculate $\Delta\theta_{WP}$. Parameters $F_{pho,max}$ and $G_2 - G_6$ were fitted using a non-linear least-square approach.

Data from mid-July to the end of August 2021 were used and in the fitting only data points with $K_{down} > 10$ W m^{-2} and $\Delta q > 1$ g kg^{-1} were selected (Havu et al., 2022a). After applying a bootstrapping method to randomly select seven eighths of the data for 100 times, the final parameters fitted for grass were obtained as medians with the uncertainties as follows: $F_{pho,max} = 5.497 \pm 0.110$ μmol m^{-2}s^{-1}, $G_2 = 195.019 \pm 5.601$ W m^{-2}, $G_3 = 0.741 \pm 0.008$, $G_4 = 0.413 \pm 0.015$, $G_5 = 30.000 \pm 0.000$ °C, $G_6 = 0.500 \pm 0.000$ mm^{-1}. The value of $F_{pho,max}$ is used for grass/lawn in the Beijing simulation.

Appendix E: Maximum conductance of urban green space in Beijing

Table E1. Maximum conductance (g_{max}) for each vegetated surface.

	Deciduous tree			
	Sophora japonica Linn.	*Populus tomentosa* Carr.	*Faxinus chinensis* Roxb.	*Ginkgo biloba* Linn.
Ratio[a]	26.26%	12.39%	9.44%	8.12%
g_{max} (mm s^{-1})	9.0	5.2	6.1	4.1
Reference	Xu et al. (2020)	Wang et al. (2018)	Xu et al. (2020)	Song et al. (2015)
	Evergreen tree	Grass/lawn		
	Pinus tabuliformis	*Festuca arundinacea* Schreb.	*Poa pratensis* L.	*Zoysia japonica* Steud.
g_{max} (mm s^{-1})	1.4[b]	5.4	4.0	1.6
Reference	Chen et al. (2021)	Wang et al. (2006)	Wang et al. (2006)	Wang et al. (2006)

[a] obtained from a field survey over Beijing (Ma et al., 2019)

[b] obtained by dividing maximum canopy conductance by G_1 (=3.5)

The weighted average of g_{max} is 7.0 mm s^{-1} for the deciduous tree weighted by the population ratio of each species (Table E1). The average g_{max} for grass is 3.7 mm s^{-1}. Note that when the species in the modelled area are known, we suggest the g_{max} is selected accordingly. Here, we seek values that can represent the overall vegetation over the urban area in Beijing, and therefore the average is taken from different species.

Appendix F: Comparison of parameters for modelling domain with different radii

Table F1. Land surface fraction for modelling domain with different radii, where "Paved" denotes paved surface, "Bldgs" buildings, "EveTr" evergreen tree, "DecTr" deciduous tree, "Grass" grassland and lawn, "Bsoil" bare soil, "Water" water body.

	Radius (m)			
	500	750	1000	1500
Fr_Paved	0.39	0.32	0.46	0.46
Fr_Bldgs	0.18	0.21	0.24	0.24
Fr_EveTr	0.04	0.04	0.02	0.02
Fr_DecTr	0.18	0.18	0.11	0.01
Fr_Grass	0.20	0.24	0.16	0.17
Fr_Bsoil	0	0	0	0
Fr_Water	0.01	0.01	0.01	0.01

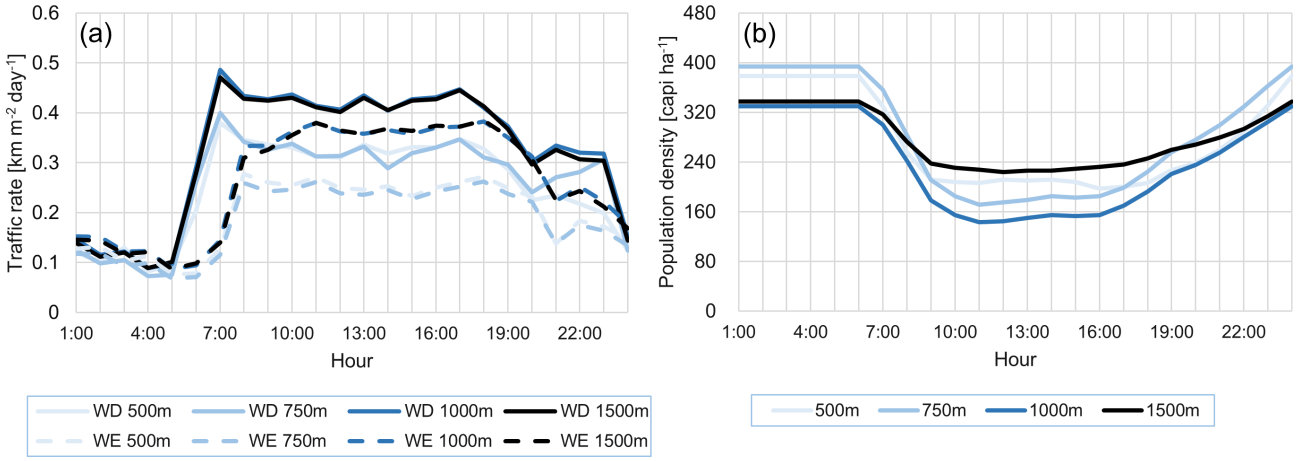

Figure F1. Diurnal cycles of (a) traffic rate and (b) population density for modelling domain with different radii, where WD denotes weekday and WE weekday.

Code and data availability. The data sets are openly available, including the complete model cases of SUEWS, the meteorological, radiation, and turbulent flux measurements, codes for LAI model optimization using CMA-ES, and codes to reproduce the statistics and figures (Zheng et al., 2022).

Author contributions. YZ, MH, HL and LJ conceptualized the study. YZ performed the SUEWS model cases, analyzed the results, and prepared the figures. HL, XC, YW, and JA collected the data. HSL performed the fitting of maximum photosynthetic rate. LJ and HL supervised the study. All authors contributed to writing and preparing the manuscript.

Competing interests. Leena Järvi is a member of the editorial board of Geoscientific Model Development. The peer-review process was guided by an independent editor, and the authors have also no other competing interests to declare.

Acknowledgements. This study is funded by National Natural Science Foundation of China (Grant No. 42161144010), China Scholarship Council (Grant No. 202104910363), Tiina and Antti Herlin Foundation (Grant No. 20200027), the Academy of Finland (Grant Nos. 321527 and 337549), and the Strategic Research Council established within the Academy of Finland (Grant No. 335201). We sincerely appreciate Mr. Weiyi Zuo from Institute of Acoustics, Chinese Academy of Sciences for his significant technical support in realizing CMA-ES method in this study.

References

Alexander, P. J., Bechtel, B., Chow, W. T., Fealy, R., and Mills, G.: Linking urban climate classification with an urban energy and water budget model: Multi–site and multi–seasonal evaluation, Urban Climate, 17, 196–215, https://doi.org/10.1016/j.uclim.2016.08.003, 2016.

Alvarez, R. and Weilenmann, M.: Effect of low ambient temperature on fuel consumption and pollutant and CO2 emissions of hybrid electric vehicles in real-world conditions, Fuel, 97, 119–124, https://doi.org/10.1016/j.fuel.2012.01.022, 2012.

Ao, X., Grimmond, C., Liu, D., Han, Z., Hu, P., Wang, Y., Zhen, X., and Tan, J.: Radiation fluxes in a business district of Shanghai, China, Journal of Applied Meteorology and Climatology, 55, 2451–2468, https://doi.org/10.1175/jamc-d-16-0082.1, 2016.

Ao, X., Grimmond, C., Ward, H., Gabey, A., Tan, J., Yang, X.-Q., Liu, D., Zhi, X., Liu, H., and Zhang, N.: Evaluation of the Surface Urban Energy and Water balance Scheme (SUEWS) at a dense urban site in Shanghai: Sensitivity to anthropogenic heat and irrigation, Journal of Hydrometeorology, 19, 1983–2005, https://doi.org/10.1175/jhm-d-18-0057.1, 2018.

Awal, M., Ohta, T., Matsumoto, K., Toba, T., Daikoku, K., Hattori, S., Hiyama, T., and Park, H.: Comparing the carbon sequestration capacity of temperate deciduous forests between urban and rural landscapes in central Japan, Urban Forestry Urban Greening, 9, 261–270, https://doi.org/10.1016/j.ufug.2010.01.007, 2010.

Best, M. and Grimmond, C.: Key conclusions of the first international urban land surface model comparison project, Bulletin of the American Meteorological Society, 96, 805–819, https://doi.org/10.1175/bams-d-14-00122.1, 2015.

Best, M. and Grimmond, C.: Modeling the partitioning of turbulent fluxes at urban sites with varying vegetation cover, Journal of Hydrometeorology, 17, 2537–2553, https://doi.org/10.1175/jhm-d-15-0126.1, 2016.

Björkegren, A. and Grimmond, C.: Net carbon dioxide emissions from central London, Urban Climate, 23, 131–158, https://doi.org/10.1016/j.uclim.2016.10.002, 2018.

BMBS: Beijing Statistical Yearbook, Beijing Municipal Bureau of Statistics, China Statistics Press, 2017.

Boegh, E., Soegaard, H., Broge, N., Hasager, C., Jensen, N., Schelde, K., and Thomsen, A.: Airborne multispectral data for quantifying leaf area index, nitrogen concentration, and photosynthetic efficiency in agriculture, Remote Sensing of Environment, 81, 179–193, https://doi.org/10.1016/s0034-4257(01)00342-x, 2002.

Chen, F., Kusaka, H., Bornstein, R., Ching, J., Grimmond, C., Grossman-Clarke, S., Loridan, T., Manning, K. W., Martilli, A., and Miao, S.: The integrated WRF/urban modelling system: development, evaluation, and applications to urban environmental problems, International Journal of Climatology, 31, 273–288, https://doi.org/10.1002/joc.2158, 2011.

Chen, S., Chen, Z., and Zhang, Z.: The canopy stomatal conductance characteristics of Pinus tabulaeformis and Acer truncatum and their environmental responses in the mountain area of Beijing (in Chinese), Chinese Journal of Plant Ecology, 45, 1329–1340, https://doi.org/10.17521/cjpe.2021.0198, 2021.

Cheng, X., Liu, X., Liu, Y., and Hu, F.: Characteristics of CO2 concentration and flux in the Beijing urban area, Journal of Geophysical Research: Atmospheres, 123, 1785–1801, https://doi.org/10.1002/2017jd027409, 2018.

Christen, A., Coops, N., Crawford, B., Kellett, R., Liss, K., Olchovski, I., Tooke, T., Van Der Laan, M., and Voogt, J.: Validation of modeled carbon-dioxide emissions from an urban neighborhood with direct eddy-covariance measurements, Atmospheric Environment, 45, 6057–6069, https://doi.org/10.1016/j.atmosenv.2011.07.040, 2011.

Chu, H., Luo, X., Ouyang, Z., Chan, W. S., Dengel, S., Biraud, S. C., Torn, M. S., Metzger, S., Kumar, J., and Arain, M. A.: Representativeness of Eddy-Covariance flux footprints for areas surrounding AmeriFlux sites, Agricultural and Forest Meteorology, 301, 108 350, https://doi.org/10.1016/j.agrformet.2021.108350, 2021.

Crawford, B. and Christen, A.: Spatial source attribution of measured urban eddy covariance CO2 fluxes, Theoretical and Applied Climatology, 119, 733–755, https://doi.org/10.1007/s00704-014-1124-0, 2015.

Cucchi, M., Weedon, G. P., Amici, A., Bellouin, N., Lange, S., Müller Schmied, H., Hersbach, H., and Buontempo, C.: Near surface meteorological variables from 1979 to 2019 derived from bias-corrected reanalysis, https://doi.org/10.24381/cds.20d54e34, (Version 2.0, accessed on 11-May-2022), 2021.

Cui, Y., Zhang, W., Wang, C., Streets, D. G., Xu, Y., Du, M., and Lin, J.: Spatiotemporal dynamics of CO2 emissions from central heating supply in the North China Plain over 2012–2016 due to natural gas usage, Applied Energy, 241, 245–256, https://doi.org/10.1016/j.apenergy.2019.03.060, 2019.

Demuzere, M., Harshan, S., Järvi, L., Roth, M., Grimmond, C., Masson, V., Oleson, K., Velasco, E., and Wouters, H.: Impact of urban canopy models and external parameters on the modelled urban energy balance in a tropical city, Quarterly Journal of the Royal Meteorological Society, 143, 1581–1596, https://doi.org/10.1002/qj.3028, 2017.

Dou, J., Grimmond, S., Cheng, Z., Miao, S., Feng, D., and Liao, M.: Summertime surface energy balance fluxes at two Beijing sites, International Journal of Climatology, 39, 2793–2810, https://doi.org/10.1002/joc.5989, 2019.

Du, M., Wang, X., Peng, C., Shan, Y., Chen, H., Wang, M., and Zhu, Q.: Quantification and scenario analysis of CO2 emissions from the central heating supply system in China from 2006 to 2025, Applied Energy, 225, 869–875, https://doi.org/10.1016/j.apenergy.2018.05.064, 2018.

Falge, E., Baldocchi, D., Olson, R., Anthoni, P., Aubinet, M., Bernhofer, C., Burba, G., Ceulemans, R., Clement, R., and Dolman, H.: Gap filling strategies for defensible annual sums of net ecosystem exchange, Agricultural and forest meteorology, 107, 43–69, https://doi.org/10.1016/j.agrformet.2006.03.003, 2001.

Fiorella, R. P., Bares, R., Lin, J. C., Ehleringer, J. R., and Bowen, G. J.: Detection and variability of combustion-derived vapor in an urban basin, Atmospheric Chemistry and Physics, 18, 8529–8547, https://doi.org/10.5194/acp-18-8529-2018, 2018.

Foken, T. and Wichura, B.: Tools for quality assessment of surface-based flux measurements, Agricultural and Forest Meteorology, 78, 83–105, https://doi.org/10.1016/0168-1923(95)02248-1, 1996.

Fontaras, G., Zacharof, N.-G., and Ciuffo, B.: Fuel consumption and CO2 emissions from passenger cars in Europe–Laboratory versus real-world emissions, Progress in Energy and Combustion Science, 60, 97–131, https://doi.org/10.1016/j.pecs.2016.12.004, 2017.

Friedl, M. and Sulla-Menashe, D.: MCD12Q1 MODIS/Terra+Aqua Land Cover Type Yearly L3 Global 500m SIN Grid V006 [Data set], https://doi.org/10.5067/MODIS/MCD12Q1.006, (Accessed on 19-Apr-2022), 2019.

Gong, P., Chen, B., Li, X., Liu, H., Wang, J., Bai, Y., Chen, J., Chen, X., Fang, L., and Feng, S.: Mapping essential urban land use categories in China (EULUC-China): Preliminary results for 2018, https://doi.org/10.1016/j.scib.2019.12.007, 2020.

Grimmond, C. and Oke, T.: Heat storage in urban areas: Local-scale observations and evaluation of a simple model, Journal of Applied Meteorology, 38, 922–940, https://doi.org/10.1175/1520-0450(1999)038<0922:HSIUAL>2.0.CO;2, 1999.

Grimmond, C. and Oke, T.: Progress in measuring and observing the urban atmosphere, Theoretical and Applied Climatology, 84, 3–22, https://doi.org/10.1007/s00704-005-0140-5, 2006.

Grimmond, C. S. B., Blackett, M., Best, M., Barlow, J., Baik, J., Belcher, S., Bohnenstengel, S., Calmet, I., Chen, F., and Dandou, A.: The International Urban Energy Balance Models Comparison Project: First Results from Phase 1, Journal of applied meteorology and climatology, 49, 1268–1292, https://doi.org/10.1175/2010jamc2354.1, 2010.

Hansen, N., Auger, A., Ros, R., Finck, S., and Pošík, P.: Comparing results of 31 algorithms from the black-box optimization benchmarking BBOB-2009, in: Proceedings of the 12th annual conference companion on Genetic and evolutionary computation, pp. 1689–1696, https://doi.org/10.1145/1830761.1830790, 2010.

Havu, M., Kulmala, L., Kolari, P., Vesala, T., Riikonen, A., and Järvi, L.: Carbon sequestration potential of street tree plantings in Helsinki, Biogeosciences, 19, 2121–2143, https://doi.org/10.5194/bg-19-2121-2022, 2022a.

Havu, M., Lee, H. S., Soininen, J., and Järvi, L.: Spatial variability of biogenic CO2 flux in Helsinki in 2020 (Version 1)[Data set], Zenodo, https://doi.org/https://doi.org/10.5281/zenodo.7198140, 2022b.

Hersbach, H., Bell, B., Berrisford, P., Hirahara, S., Horányi, A., Muñoz-Sabater, J., Nicolas, J., Peubey, C., Radu, R., Schepers, D., et al.: The ERA5 global reanalysis, Quarterly Journal of the Royal Meteorological Society, 146, 1999–2049, https://doi.org/10.1002/qj.3803, 2020.

Huete, A.: A comparison of vegetation indices over a global set of TM images for EOS-MODIS, Remote Sensing of Environment, 59, 440–451, https://doi.org/10.1016/s0034-4257(96)00112-5, 1997.

Järvi, L., Grimmond, C., McFadden, J., Christen, A., Strachan, I., Taka, M., Warsta, L., and Heimann, M.: Warming effects on the urban hydrology in cold climate regions, Scientific reports, 7, 1–8, https://doi.org/10.1038/s41598-017-05733-y, 2017.

Jiang, X., Zhang, C., Gao, H., and Miao, S.: Impacts of urban albedo change on urban heat island in Beijing-A case study (in Chinese), Acta Meteorologica Sinica, 65, 301–307, https://doi.org/10.1002/jrs.1570, 2007.

Johansson, E. and Emmanuel, R.: The influence of urban design on outdoor thermal comfort in the hot, humid city of Colombo, Sri Lanka, International journal of biometeorology, 51, 119–133, https://doi.org/10.1007/s00484-006-0047-6, 2006.

Järvi, L., Grimmond, C., and Christen, A.: The Surface Urban Energy and Water Balance Scheme (SUEWS): Evaluation in Los Angeles and Vancouver, Journal of Hydrology, 411, 219–237, https://doi.org/10.1016/j.jhydrol.2011.10.001, 2011.

Järvi, L., Grimmond, C. S. B., Taka, M., Nordbo, A., Setälä, H., and Strachan, I. B.: Development of the Surface Urban Energy and Water Balance Scheme (SUEWS) for cold climate cities, Geoscientific Model Development, 7, 1691–1711, https://doi.org/10.5194/gmd-7-1691-2014, 2014.

Järvi, L., Havu, M., Ward, H. C., Bellucco, V., McFadden, J. P., Toivonen, T., Heikinheimo, V., Kolari, P., Riikonen, A., and Grimmond, C. S. B.: Spatial modeling of local-scale biogenic and anthropogenic carbon dioxide emissions in Helsinki, Journal of Geophysical Research: Atmospheres, 124, 8363–8384, https://doi.org/10.1029/2018jd029576, 2019.

Karsisto, P., Fortelius, C., Demuzere, M., Grimmond, C. S. B., Oleson, K., Kouznetsov, R., Masson, V., and Järvi, L.: Seasonal surface urban energy balance and wintertime stability simulated using three land-surface models in the high-latitude city Helsinki, Quarterly Journal of the Royal Meteorological Society, 142, 401–417, https://doi.org/10.1002/qj.2659, 2016.

Kokkonen, T., Grimmond, C. S. B., Räty, O., Ward, H., Christen, A., Oke, T., Kotthaus, S., and Järvi, L.: Sensitivity of Surface Urban Energy and Water Balance Scheme (SUEWS) to downscaling of reanalysis forcing data, Urban Climate, 23, 36–52, https://doi.org/10.1016/j.uclim.2017.05.001, 2018.

Kokkonen, T. V., Grimmond, S., Murto, S., Liu, H., Sundström, A.-M., and Järvi, L.: Simulation of the radiative effect of haze on the urban hydrological cycle using reanalysis data in Beijing, Atmospheric Chemistry and Physics, 19, 7001–7017, 2019.

Konopka, J., Heusinger, J., and Weber, S.: Extensive Urban Green Roof Shows Consistent Annual Net Uptake of Carbon as Documented by 5 Years of Eddy-Covariance Flux Measurements, Journal of Geophysical Research: Biogeosciences, 126, e2020JG005 879, https://doi.org/10.1029/2020jg005879, 2021.

Laine, A., Riutta, T., Juutinen, S., Väliranta, M., and Tuittila, E.-S.: Acknowledging the spatial heterogeneity in modelling/reconstructing carbon dioxide exchange in a northern aapa mire, Ecological Modelling, 220, 2646–2655, https://doi.org/10.1016/j.ecolmodel.2009.06.047, 2009.

Liu, H., Feng, J., Järvi, L., and Vesala, T.: Four-year (2006–2009) eddy covariance measurements of CO2 flux over an urban area in Beijing, Atmospheric Chemistry and Physics, 12, 7881–7892, 2012.

Liu, S., Pang, H., Zhang, N., Xing, M., Wu, S., and Hou, S.: Temporal variations of the contribution of combustion-derived water vapor to urban humidity during winter in Xi'an, China, Science of The Total Environment, 830, 154 711, https://doi.org/10.2139/ssrn.3994594, 2022.

Liu, Y., Liu, H., Du, Q., and Xu, L.: Multi-level CO2 fluxes over Beijing megacity with the eddy covariance method, Atmospheric and Oceanic Science Letters, 14, 100 079, https://doi.org/10.1016/j.aosl.2021.100079, 2021.

Loridan, T., Grimmond, C., Offerle, B. D., Young, D. T., Smith, T. E., Järvi, L., and Lindberg, F.: Local-scale urban meteorological parameterization scheme (LUMPS): longwave radiation parameterization and seasonality-related developments, Journal of Applied Meteorology and Climatology, 50, 185–202, https://doi.org/10.1175/2010jamc2474.1, 2011.

Lu, P., Yu, Q., Liu, J., and Lee, X.: Advance of tree-flowering dates in response to urban climate change, Agricultural and Forest Meteorology, 138, 120–131, https://doi.org/10.1016/j.agrformet.2006.04.002, 2006.

Luo, Z., Sun, O. J., Ge, Q., Xu, W., and Zheng, J.: Phenological responses of plants to climate change in an urban environment, Ecological Research, 22, 507–514, https://doi.org/10.1007/s11284-006-0044-6, 2007.

Ma, J.: The study on urban forest structure and eco-service in the Sixth Ring Road of Beijing, Thesis, https://doi.org/10.27625/d.cnki.gzlky.2019.000083, 2019.

Ma, J., Jia, B., Zhang, W., Liu, X., Li, X., and Liu, J.: The characteristics of urban forest structure within the Sixth Ring Road of Beijing, Chinese Journal of Ecology, 38, 2318–2325, https://doi.org/10.13292/j.1000-4890.201908.035, 2019.

Marcotullio, P. J., Sarzynski, A., Albrecht, J., Schulz, N., and Garcia, J.: The geography of global urban greenhouse gas emissions: An exploratory analysis, Climatic Change, 121, 621–634, https://doi.org/10.1007/s10584-013-0977-z, 2013.

Masek, J., Vermote, E., Saleous, N., Wolfe, R., Hall, F., Huemmrich, K., Gao, F., Kutler, J., and Lim, T.-K.: A Landsat Surface Reflectance Dataset for North America, 1990–2000, IEEE Geoscience and Remote Sensing Letters, 3, 68–72, https://doi.org/10.1109/lgrs.2005.857030, 2006.

Masson, V., Le Moigne, P., Martin, E., Faroux, S., Alias, A., Alkama, R., Belamari, S., Barbu, A., Boone, A., and Bouyssel, F.: The SURFEXv7.2 land and ocean surface platform for coupled or offline simulation of earth surface variables and fluxes, Geoscientific Model Development, 6, 929–960, https://doi.org/10.5194/gmd-6-929-2013, 2013.

MHURD, M.: China urban-rural construction statistical yearbook 2016, China Statistics Press, 2018.

Miao, S., Dou, J., Chen, F., Li, J., and Li, A.: Analysis of observations on the urban surface energy balance in Beijing, Science China Earth Sciences, 55, 1881–1890, https://doi.org/10.1007/s11430-012-4411-6, 2012.

Moriwaki, R. and Kanda, M.: Seasonal and diurnal fluxes of radiation, heat, water vapor, and carbon dioxide over a suburban area, Journal of Applied Meteorology, 43, 1700–1710, https://doi.org/10.1175/jam2153.1, 2004.

Nordbo, A., Karsisto, P., Matikainen, L., Wood, C. R., and Järvi, L.: Urban surface cover determined with airborne lidar at 2 m resolution–implications for surface energy balance modelling, Urban Climate, 13, 52–72, https://doi.org/10.1016/j.uclim.2015.05.004, 2015.

Offerle, B., Grimmond, C., and Oke, T. R.: Parameterization of net all-wave radiation for urban areas, Journal of Applied Meteorology and Climatology, 42, 1157–1173, https://doi.org/10.1175/1520-0450(2003)042<1157:ponarf>2.0.co;2, 2003.

Oke, T.: The Heat Island of the Urban Boundary Layer: Characteristics, Causes and Effects, pp. 81–107, Springer, https://doi.org/10.1007/978-94-017-3686-2_5, 1995.

Omidvar, H., Sun, T., Grimmond, S., Bilesbach, D., Black, A., Chen, J., Duan, Z., Gao, Z., Iwata, H., and McFadden, J. P.: Surface Urban Energy and Water Balance Scheme (v2020a) in vegetated areas: parameter derivation and performance evaluation using FLUXNET2015 dataset, Geoscientific Model Development, 15, 3041–3078, https://doi.org/10.5194/gmd-15-3041-2022, 2022.

Pataki, D. E., Carreiro, M. M., Cherrier, J., Grulke, N. E., Jennings, V., Pincetl, S., Pouyat, R. V., Whitlow, T. H., and Zipperer, W. C.: Coupling biogeochemical cycles in urban environments: ecosystem services, green solutions, and misconceptions, Frontiers in Ecology and the Environment, 9, 27–36, https://doi.org/10.1890/090220, 2011.

Peters, E. B. and McFadden, J. P.: Continuous measurements of net CO2 exchange by vegetation and soils in a suburban landscape, Journal of Geophysical Research: Biogeosciences, 117, https://doi.org/10.1029/2011jg001933, 2012.

Prairie, Y. T. and Duarte, C. M.: Direct and indirect metabolic CO2 release by humanity, Biogeosciences, 4, 215–217, https://doi.org/10.5194/bg-4-215-2007, 2007.

Qian, Y., Chakraborty, T., Li, J., Li, D., He, C., Sarangi, C., Chen, F., Yang, X., and Leung, L. R.: Urbanization Impact on Regional Climate and Extreme Weather: Current Understanding, Uncertainties, and Future Research Directions, Advances in Atmospheric Sciences, pp. 1–42, https://doi.org/10.1007/s00376-021-1371-9, 2022.

Rebmann, C., Göckede, M., Foken, T., Aubinet, M., Aurela, M., Berbigier, P., Bernhofer, C., Buchmann, N., Carrara, A., and Cescatti, A.: Quality analysis applied on eddy covariance measurements at complex forest sites using footprint modelling, Theoretical and Applied Climatology, 80, 121–141, https://doi.org/10.1007/s00704-004-0095-y, 2005.

Salmon, O. E., Shepson, P. B., Ren, X., Marquardt Collow, A. B., Miller, M. A., Carlton, A. G., Cambaliza, M. O., Heimburger, A., Morgan, K. L., and Fuentes, J. D.: Urban emissions of water vapor in winter, Journal of Geophysical Research: Atmospheres, 122, 9467–9484, https://doi.org/10.1002/2016jd026074, 2017.

Sarangi, C., Tripathi, S., Qian, Y., Kumar, S., and Ruby Leung, L.: Aerosol and urban land use effect on rainfall around cities in Indo-Gangetic Basin from observations and cloud resolving model simulations, Journal of Geophysical Research: Atmospheres, 123, 3645–3667, https://doi.org/10.1002/2017jd028004, 2018.

Song, Y., Li, F., Wang, X., Xu, C., Zhang, J., Liu, X., and Zhang, H.: The effects of urban impervious surfaces on eco-physiological characteristics of Ginkgo biloba: A case study from Beijing, China, Urban Forestry Urban Greening, 14, 1102–1109, https://doi.org/10.1016/j.ufug.2015.10.008, 2015.

Stagakis, S., Feigenwinter, C., Vogt, R., and Kalberer, M.: A high-resolution monitoring approach of urban CO2 fluxes. Part 1-bottom-up model development, Science of The Total Environment, p. 160216, https://doi.org/10.2139/ssrn.4172744, 2022.

Sun, T. and Grimmond, S.: A Python-enhanced urban land surface model SuPy (SUEWS in Python, v2019.2): development, deployment and demonstration, Geoscientific Model Development, 12, 2781–2795, https://doi.org/10.5194/gmd-12-2781-2019, 2019.

Tan, J., Zheng, Y., Tang, X., Guo, C., Li, L., Song, G., Zhen, X., Yuan, D., Kalkstein, A. J., and Li, F.: The urban heat island and its impact on heat waves and human health in Shanghai, International Journal of Biometeorology, 54, 75–84, https://doi.org/10.1007/s00484-009-0256-x, 2010.

United Nations Department of Economic and Social Affairs: World Urbanization Prospects: The 2018 Revision, United Nations, https://doi.org/10.18356/b9e995fe-en, 2019.

Velasco, E. and Roth, M.: Cities as net sources of CO2: Review of atmospheric CO2 exchange in urban environments measured by eddy covariance technique, Geography Compass, 4, 1238–1259, https://doi.org/10.1111/j.1749-8198.2010.00384.x, 2010.

Wang, L., Fan, S., Hu, F., Miao, S., Yang, A., Li, Y., Liu, J., Liu, C., Chen, S., Ho, H. C., Duan, Z., Gao, Z., and Yang, Y.: Vertical gradient variations in radiation budget and heat fluxes in the urban boundary layer: A comparison study between polluted and clean air episodes in Beijing during winter, Journal of Geophysical Research: Atmospheres, 125, https://doi.org/10.1029/2020jd032478, 2020.

Wang, Y., Yang, J., and Han, L.: Effects of different irrigation volume on photosynthesis of turfgrass (in Chinese), Journal of Beijing Forestry University, pp. 26–31, https://doi.org/CNKI:SUN:BJLY.0.2006-S1-006, 2006.

Wang, Y., Li, G., Di, N., Clothier, B., Duan, J., Li, D., Jia, L., Xi, B., and Ma, F.: Leaf phenology variation within the canopy and its relationship with the transpiration of Populus tomentosa under plantation conditions, Forests, 9, 603, https://doi.org/10.3390/f9100603, 2018.

Wang, Y., Chang, Q., and Li, X.: Promoting sustainable carbon sequestration of plants in urban greenspace by planting design: A case study in parks of Beijing, Urban Forestry Urban Greening, 64, 127 291, https://doi.org/10.1016/j.ufug.2021.127291, 2021.

Ward, H., Evans, J. G., and Grimmond, C. S. B.: Multi-season eddy covariance observations of energy, water and carbon fluxes over a suburban area in Swindon, UK, Atmospheric Chemistry and Physics, 13, 4645–4666, https://doi.org/10.5194/acp-13-4645-2013, 2013.

Ward, H. C., Kotthaus, S., Järvi, L., and Grimmond, C. S. B.: Surface Urban Energy and Water Balance Scheme (SUEWS): development and evaluation at two UK sites, Urban Climate, 18, 1–32, https://doi.org/10.1016/j.uclim.2016.05.001, 2016.

Watts, N., Adger, W. N., Agnolucci, P., Blackstock, J., Byass, P., Cai, W., Chaytor, S., Colbourn, T., Collins, M., and Cooper, A.: Health and climate change: policy responses to protect public health, The lancet, 386, 1861–1914, https://doi.org/10.1016/S0140-6736(15)60854-6, 2015.

Wen, Y., Zhang, S., Zhang, J., Bao, S., Wu, X., Yang, D., and Wu, Y.: Mapping dynamic road emissions for a megacity by using open-access traffic congestion index data, Applied Energy, 260, 114 357, https://doi.org/10.1016/j.apenergy.2019.114357, 2020.

Wen, Y., Wu, R., Zhou, Z., Zhang, S., Yang, S., Wallington, T. J., Shen, W., Tan, Q., Deng, Y., and Wu, Y.: A data-driven method of traffic emissions mapping with land use random forest models, Applied Energy, 305, 117 916, https://doi.org/10.1016/j.apenergy.2021.117916, 2022.

Xu, Y., Li, S., Yuan, X., and Feng, Z.: Emission characteristics of biogenic volatile compounds (BVOCs) from common greening tree species in northern China and their correlations with photosynthetic parameters (in Chinese), Environmental Science, 41, 3518–3526, https://doi.org/10.13227/j.hjkx.202001180, 2020.

Yang, D., Zhang, S., Niu, T., Wang, Y., Xu, H., Zhang, K. M., and Wu, Y.: High-resolution mapping of vehicle emissions of atmospheric pollutants based on large-scale, real-world traffic datasets, Atmospheric Chemistry and Physics, 19, 8831–8843, https://doi.org/10.5194/acp-19-8831-2019, 2019.

Zhang, D., Gao, J., Tang, D., Wu, X., Shi, J., Chen, J., Peng, Y., Zhang, S., and Wu, Y.: Switching on auxiliary devices in vehicular fuel efficiency tests can help cut CO2 emissions by millions of tons, One Earth, 4, 135–145, https://doi.org/10.1016/j.oneear.2020.12.010, 2021.

Zhang, H., Zhou, L., Huang, X., and Zhang, X.: Decarbonizing a large City's heating system using heat pumps: A case study of Beijing, Energy, 186, 115 820, https://doi.org/10.1016/j.energy.2019.07.150, 2019.

Zhang, S., Wu, Y., Liu, H., Huang, R., Yang, L., Li, Z., Fu, L., and Hao, J.: Real-world fuel consumption and CO2 emissions of urban public buses in Beijing, Applied Energy, 113, 1645–1655, https://doi.org/10.1016/j.apenergy.2013.09.017, 2014.

Zhang, X., Mi, F., Lu, N., Yan, N., Kuglerova, L., Yuan, S., Peng, Q., and Ma, O. Z.: Green space water use and its impact on water resources in the capital region of China, Physics and Chemistry of the Earth, Parts A/B/C, 101, 185–194, https://doi.org/10.1016/j.pce.2017.02.001, 2017.

Zhang, Y., Yin, P., Li, X., Niu, Q., Wang, Y., Cao, W., Huang, J., Chen, H., Yao, X., and Yu, L.: The divergent response of vegetation phenology to urbanization: A case study of Beijing city, China, Science of The Total Environment, 803, 150 079, https://doi.org/10.1016/j.scitotenv.2021.150079, 2022.

Zhao, X., Zhou, Y., Chen, W., Li, X., Li, X., and Li, D.: Mapping hourly population dynamics using remotely sensed and geospatial data: a case study in Beijing, China, GIScience Remote Sensing, 58, 717–732, https://doi.org/10.1080/15481603.2021.1935128, 2021.

Zheng, Y., Liu, H., and Cheng, X.: Datasets for simulating heat and CO2 fluxes in Beijing using SUEWS V2020b [Data set], https://doi.org/10.5281/zenodo.7427360, 2022.

Zhu, X., Ni, G., Cong, Z., Sun, T., and Li, D.: Impacts of surface heterogeneity on dry planetary boundary layers in an urban-rural setting, Journal of Geophysical Research: Atmospheres, 121, 12,164–12,179, https://doi.org/10.1002/2016jd024982, 2016.